ApJ, submitted; July 15, 2016
Preprint typeset using LaTeX style emulateapj v. 01/23/15

arXiv:1607.03907v1 [astro-ph.HE] 13 Jul 2016

EXTERNAL COMPTON SCATTERING IN BLAZAR JETS AND THE LOCATION OF THE GAMMA-RAY EMITTING REGION

Justin D. Finke
U.S. Naval Research Laboratory, Code 7653, 4555 Overlook Ave. SW, Washington, DC, 20375-5352

ApJ, submitted; July 15, 2016

ABSTRACT

I study the location of the γ-ray emission in blazar jets by creating a Compton-scattering approximation valid for all anisotropic radiation fields in the Thomson through Klein-Nishina regimes, which is highly accurate and can speed up numerical calculations by up to a factor ~ 10. I apply this approximation to synchrotron self-Compton, and external Compton-scattering of photons from the accretion disk, broad-line region (BLR), and dust torus. I use a stratified BLR model and include detailed Compton-scattering calculations of a spherical and flattened BLR. I create two dust torus models, one where the torus is an annulus, and one where it is an extended disk. I present detailed calculations of the photoabsorption optical depth using my detailed BLR and dust torus models, including the full angle dependence. I apply these calculations to the emission from a relativistically moving blob traveling through these radiation fields. The ratio of γ-ray to optical flux produces a predictable pattern that could help locate the γ-ray emission region. I show that the bright flare from 3C 454.3 in 2010 November detected by the Fermi Large Area Telescope is unlikely to originate from a single blob inside the BLR since it moves outside the BLR in a time shorter than the flare duration, although emission by multiple blobs inside the BLR is possible; and γ-rays are unlikely to originate from outside the BLR from scattering of photons from an extended dust torus, since then the cooling timescale would be too long to explain the observed short variability.

Subject headings: quasars: general — radiation mechanisms: non-thermal — galaxies: active — galaxies: jets — gamma rays: galaxies

1. INTRODUCTION

Blazars are active galactic nuclei (AGN) with jets of nonthermal plasma moving at relativistic speeds oriented close to our line of sight. They produce nonthermal radiation across the electro-magnetic spectrum, from radio to γ rays, the lower portion of which is almost certainly produced by nonthermal synchrotron. Blazars are classified based on the strength or weakness of broad lines in their optical spectra as FSRQs or BL Lacs, respectively (e.g. Marcha et al. 1996; Landt et al. 2004), and on the location of their synchrotron peak (ν_{pk}; Abdo et al. 2010b) in νF_ν spectral energy distributions (SEDs) as low-synchrotron peaked (LSP; $\nu_{pk} < 10^{14}$ Hz), intermediate-synchrotron peaked (ISP; 10^{14} Hz $< \nu_{pk} < 10^{15}$ Hz), or high-synchrotron peaked (HSP; 10^{15} Hz $< \nu_{pk}$).

In the 0.1–300 GeV energy range, blazars dominate the sky in terms of number of associated sources (Acero et al. 2015). Hadronic models for γ-ray production in these sources often face difficulties due to requiring excessive jet powers, especially for FSRQs and LSPs (Böttcher et al. 2013; Zdziarski & Böttcher 2015; Petropoulou & Dimitrakoudis 2015; Petropoulou & Dermer 2016), although there are some examples, especially HSPs, where jet powers are more reasonable (e.g., Cerruti et al. 2015). Inverse Compton scattering of soft photons by relativistic nonthermal electrons in the jet is usually invoked as the most likely mechanism for γ-ray production in FSRQs and some LSPs. Possible seed photons for Compton scattering include the synchrotron photons produced by the same population of electrons that produces the γ rays (known as synchrotron self-Compton, or SSC; Bloom & Marscher 1996); or seed photons from another portion of the jet (e.g., Ghisellini et al. 2005; MacDonald et al. 2015; Sikora et al. 2016); or by seed photons external to the jet entirely, for instance, from the accretion disk (Dermer et al. 1992; Dermer & Schlickeiser 1993), broad line region (BLR; Sikora et al. 1994), or dust torus (Kataoka et al. 1999; Błażejowski et al. 2000) in the object; or from the cosmic microwave background (CMB; Böttcher et al. 2008; Yan et al. 2012; Meyer et al. 2015; Sanchez et al. 2015; Zacharias & Wagner 2016). The dominant seed photon source depends critically on the location in the jet of the emitting region. In order of increasing distance from the black hole, the dominant external seed photon source could be the accretion disk, the BLR, the dust torus, and/or the CMB. The dominant seed photon source, and the location of the primary emitting region, is an important topic in the understanding of blazar jets that has not yet been resolved. I endeavor to make progress in answering this question by providing detailed calculations of Compton scattering of the relevant external radiation fields.

Calculations of Compton scattering of various external radiation fields (external Compton or EC hereafter) using the full Compton cross section, valid in the Thomson and extreme Klein-Nishina regimes, including anisotropic external radiation fields, have been explored by many authors (e.g., Böttcher et al. 1997; Böttcher & Bloom 2000; Dermer et al. 2009;

justin.finke@nrl.navy.mil

Hutter & Spanier 2011; Hunger & Reimer 2016). These calculations can be quite numerically intense, especially if calculations are repeated numerous times in, for example, fitting routines (Finke et al. 2008; Mankuzhiyil et al. 2010, 2011; Yan et al. 2013; Cerruti et al. 2013a) or multi-zone models (e.g., Jamil & Böttcher 2012; Joshi et al. 2014). Often, δ-function approximations, valid in the Thomson regime, are used to approximate Compton scattering processes (e.g., Dermer et al. 1992; Dermer & Schlickeiser 1993). In these approximations, *all* of the scattering photons are assumed to have the same energy, that of the mean scattered photon energy. A δ-function approximation valid at all energies, in the Thomson through extreme Klein-Nishina regimes, was developed by Moderski et al. (2005) for isotropic radiation fields, which I made use of recently to compute theoretical power spectral densities and Fourier-frequency dependent time lags of blazar light curves (Finke & Becker 2015). In the present manuscript, I generalize the δ-function approximation of Moderski et al. (2005) to anisotropic radiation fields (Section 2) and apply it to EC for several external isotropic and anisotropic external radiation fields (Section 3), and, for completeness, to SSC (Section 4), all in the context of relativistic jets. Researchers may find this δ-function approximation useful for Compton-scattering calculations in other astrophysical contexts besides blazars, such as microquasars (e.g., Gupta et al. 2006; Dubus et al. 2008, 2010; Zdziarski et al. 2014), colliding winds of massive stars (e.g., Reimer et al. 2006), or gamma-ray bursts (e.g., Lu et al. 2015). The speed and accuracy of the approximations are explored in Section 5. The δ-function approximations are used to derive the beaming pattern for the scattering of various external radiation fields by relativistic jets in Section 6.

Another process necessary to the Compton-scattering model for blazar jet emission is $\gamma\gamma$ absorption. The interaction of γ rays with soft photons from the accretion disk, BLR, and dust torus can limit the escape of γ rays. This process is explored in Section 7. As the γ-ray emitting region moves at relativistic speeds, it travels through regions where various external radiation fields dominate the Compton scattering process. In Section 8 I look at the effect this would have on the ratio of γ-ray to optical flux that one would expect as a function of time. This can give critical clues to the location of the γ-ray emitting region in blazars. In particular, I apply the calculations presented here to the optical and γ-ray light curves of the giant flare in 3C 454.3 in 2010 November. I conclude with a summary in Section 9. In Appendix A, I present a simple model for determining the luminosities and radii of line emission in a stratified BLR based on a composite quasar spectrum from the Sloan Digital Sky Survey (SDSS).

2. DELTA FUNCTION SCATTERING APPROXIMATION

2.1. *Compton Scattering Cross Section in the Head-On Approximation*

The emissivity from Compton scattering is given by

$$\epsilon_s\, j(\epsilon_s,\Omega_s) = m_e c^3 \epsilon_s^2 \int d\Omega \int d\epsilon\; n_{ph}(\epsilon,\Omega) \times \int d\Omega_e \int d\gamma\; n_e(\gamma,\Omega_e) \times (1-\cos\psi)\frac{d\sigma}{d\epsilon_s d\Omega_s} \quad (1)$$

(e.g., Dermer & Menon 2009) where m_e is the electron mass, c is the speed of light, ϵ_s is the scattered photon energy in $m_e c^2$ units, $n_{ph}(\epsilon,\Omega)$ is the number density of incident ("seed") photons with energies between ϵ and $\epsilon + d\epsilon$ and solid angles between Ω and $\Omega + d\Omega$, $n_e(\gamma,\Omega_e)$ is the number density of incident electrons with Lorentz factors between γ and $\gamma + d\gamma$ and solid angles between Ω_e and $\Omega_e + d\Omega_e$, $d\sigma/(d\epsilon_s d\Omega_s)$ is the differential cross section per scattered photon energy and solid angle, and ψ is the angle between the direction of the incident photon and electron.

In the "head-on" approximation, $\epsilon \ll 1 \ll \gamma$, and photons are scattered in approximately the same direction as the incident electrons (Reynolds 1982; Dermer & Schlickeiser 1993; Dermer et al. 2009), so that

$$\frac{d\sigma}{d\epsilon_s d\Omega_s} \approx \frac{d\sigma}{d\epsilon_s}\delta(\Omega_s - \Omega_e) \quad (2)$$

where

$$\frac{d\sigma}{d\epsilon_s} = \int d\Omega_s \frac{d\sigma}{d\epsilon_s d\Omega_s} = \frac{3\sigma_{\rm T}}{8\gamma\bar{\epsilon}}\; \Xi(\bar{\epsilon},y) \times H\left(\epsilon_s; \frac{\bar{\epsilon}}{2\gamma}, \frac{2\gamma\bar{\epsilon}}{1+2\bar{\epsilon}}\right)\,, \quad (3)$$

$$\Xi(\bar{\epsilon},y) = 1 - y + \frac{1}{1-y} - \frac{2y}{\bar{\epsilon}(1-y)} + \left[\frac{y}{\bar{\epsilon}(1-y)}\right]^2\,, \quad (4)$$

$$\bar{\epsilon} = \gamma\epsilon(1-\cos\psi)\,, \quad (5)$$

$$y = \frac{\epsilon_s}{\gamma}\,, \quad (6)$$

and

$$H(x;a,b) = \begin{cases} 1 & a < x < b \\ 0 & \text{otherwise} \end{cases}\,. \quad (7)$$

If the incident photon travels in a direction given by azimuthal and polar angles ϕ and $\theta = \arccos(\mu)$, respectively, and the scattered photon travels in a direction given by the azimuthal and polar angles, ϕ_s and $\theta_s = \arccos(\mu_s)$, respectively, then

$$\cos\psi = \mu\mu_s + \sqrt{1-\mu^2}\sqrt{1-\mu_s^2} \times \cos(\phi - \phi_s)\,. \quad (8)$$

For the remainder of this paper, I define the coordinate system so that $\phi_s = 0$. The geometry of the head-on approximation is illustrated in Figure 1. The head-on

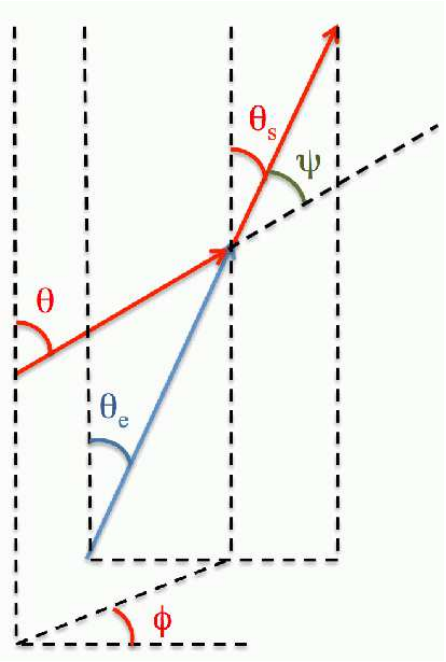

FIG. 1.— An illustration of the geometry of scattering in the head-on approximation.

approximation implies

$$\epsilon_s\, j(\epsilon_s,\Omega_s) \approx m_e c^3 \epsilon_s^2 \int d\Omega \int d\epsilon\; n_{ph}(\epsilon,\Omega) \times \int d\gamma\; n_e(\gamma,\Omega_s)(1-\cos\psi)\frac{d\sigma}{d\epsilon_s}\;. \quad (9)$$

It will be useful to compute the total Compton-scattering cross section, which is

$$\sigma(\bar{\epsilon}) = \int d\epsilon_s \frac{d\sigma}{d\epsilon_s} = \sigma_{\rm T} S_0(\bar{\epsilon}) \quad (10)$$

where

$$S_0(x) = \frac{3}{8x^2}\left[4 + \frac{2x^2(1+x)}{(1+2x)^2} + \frac{x^2-2x-2}{x}\ln(1+2x)\right]. \quad (11)$$

This function has the asymptotes

$$S_0(x) \to 1 - 2x + \frac{26x^2}{5} - \frac{133x^3}{10} + \frac{1444x^4}{35} \quad (12)$$

for $x \ll 1$ and

$$S_0(x) \to \frac{3}{8x}\left[\ln(x) + \frac{1}{2} + \frac{1}{2}\ln(4)\right] \quad (13)$$

for $x \gg 1$, and it is plotted in Figure 2.

It will also be useful to integrate the total cross section over all angles, so that

$$\int_0^{2\pi} d\phi \int_{-1}^{1} d\mu\; (1-\mu)\; \sigma(\gamma\epsilon(1-\mu)) = \frac{3\sigma_{\rm T}(2\pi)}{8(\gamma\epsilon)^2} M_0(4\gamma\epsilon) \quad (14)$$

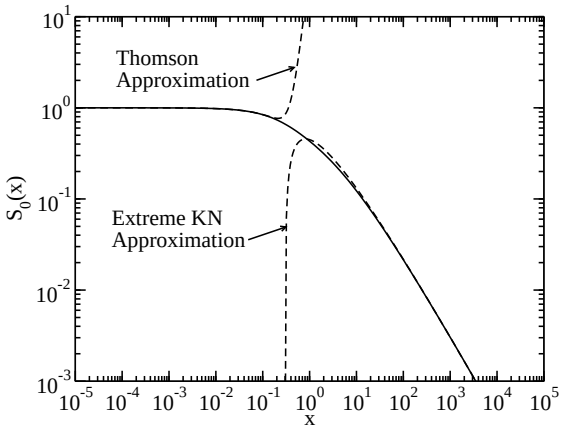

FIG. 2.— The function $S_0(x)$ given by Equation (11) and the approximations from Equations (12) ($x \ll 1$) and (13) ($x \gg 1$).

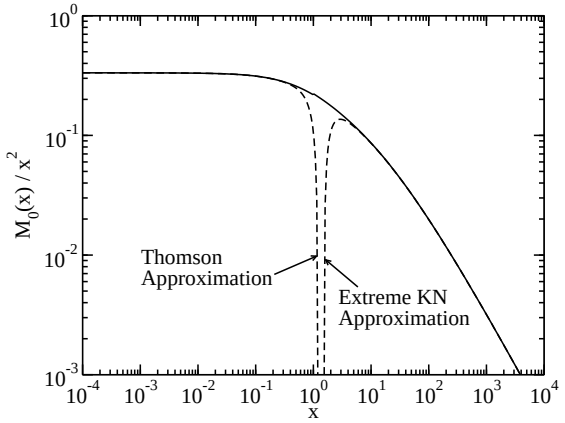

FIG. 3.— The function $M_0(x)$ given by Equation (15) and the approximations from Equations (16) ($x \ll 1$) and (17) ($x \gg 1$).

where

$$M_0(x) = 2(x+1)x\,{\rm Li}_2(-x) - \frac{1}{2}\left(\frac{x}{2}+1\right)x^2 + \left(\frac{x}{2}+4\right)(x+1)^2\ln(x+1) - 4 \quad (15)$$

and ${\rm Li}_2(x)$ is the dilogarithm function. The function $M_0(x)$ has the asymptotes

$$M_0(x) \to \frac{x^2}{3} - \frac{2x^3}{9} + \frac{13x^4}{60} - \frac{133x^5}{600} \quad (16)$$

for $x \ll 1$ and

$$M_0(x) \to \frac{x}{2}\left(\ln(x) - \frac{1}{2}\right) + 3.114\ln(x) - \ln^2\left(\frac{x}{2}\right) - 6.559 + \frac{2}{x}(2\ln(x)+3.249) \quad (17)$$

for $x \gg 1$, and it is plotted in Figure 3.

2.2. *Mean Scattered Photon Energy*

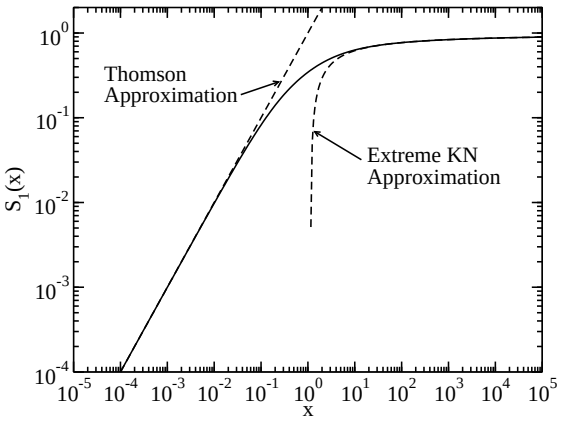

FIG. 4.— The function $S_1(x)$ defined by Equation (21) and approximations from Equation (22) for $x \ll 1$ and $x \gg 1$.

The zeroth moment of the Compton-scattering cross section is

$$\langle \epsilon_s^0 \sigma \rangle = \int d\Omega_s \int d\epsilon_s \frac{d\sigma}{d\epsilon_s d\Omega_s} = \sigma(\bar{\epsilon}) = \sigma_{\rm T} S_0(\bar{\epsilon}) \ . \quad (18)$$

The first moment is

$$\langle \epsilon_s^1 \sigma \rangle = \int d\Omega_s \int d\epsilon_s \ \epsilon_s \ \frac{d\sigma}{d\epsilon_s d\Omega_s} = \gamma \sigma_{\rm T} \left\{ S_0(\bar{\epsilon}) - \frac{3}{8\bar{\epsilon}^3} \left[\frac{\bar{\epsilon}^2}{3} \left(\frac{(1+2\bar{\epsilon})^3 - 1}{(1+2\bar{\epsilon})^3} \right) + \frac{2\bar{\epsilon}(\bar{\epsilon}^2 - \bar{\epsilon} - 1)}{1+2\bar{\epsilon}} + \ln(1+2\bar{\epsilon}) \right] \right\} \quad (19)$$

(Dermer & Schlickeiser 1993; Dermer & Menon 2009). Calculation of these and higher-order moments were performed by Coppi & Blandford (1990). The mean scattered photon energy is

$$\langle \epsilon_s \rangle = \frac{\langle \epsilon_s^1 \sigma \rangle}{\langle \epsilon_s^0 \sigma \rangle} \ . \quad (20)$$

A particularly useful quantity is the mean scattered photon energy as a fraction of the incident electron energy,

$$\langle y \rangle = \frac{\langle \epsilon_s \rangle}{\gamma} = \frac{\langle \epsilon_s^1 \sigma \rangle}{\gamma \langle \epsilon_s^0 \sigma \rangle} = S_1(\bar{\epsilon}) \quad (21)$$

where $S_1(x)$ is a function that can be computed numerically. This is a function only of the parameter $\bar{\epsilon} = \gamma\epsilon(1 - \cos\psi)$, a useful property that I will exploit in Section 2.3. The function $S_1(x)$ and its asymptotes

$$S_1(x) \rightarrow \begin{cases} x & x \ll 1 \\ 1 - 4/[3(\ln(2x) + 1/2)] & x \gg 1 \end{cases} \quad (22)$$

are plotted in Figure 4.

It will be useful to find the angle-averaged mean photon energy as a fraction of incident electron energy. This can

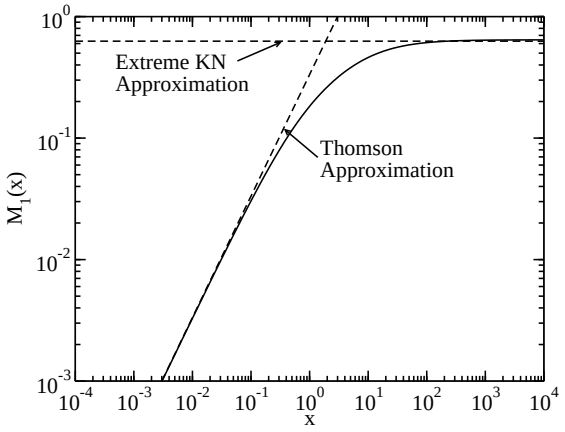

FIG. 5.— The function $M_1(x)$ defined by Equation (24) and approximations from Equation (27) for $x \ll 1$ and $x \gg 1$.

be found from

$$\langle y \rangle_{\mu,\phi} = \frac{\langle \epsilon_s \rangle_{\mu,\phi}}{\gamma} = \frac{\int_0^\infty dy \ y \ \int_0^{2\pi} d\phi \int_{-1}^1 d\mu \ (1-\mu) \ \frac{d\sigma}{d\epsilon_s}}{\int_0^\infty dy \ \int_0^{2\pi} d\phi \int_{-1}^1 d\mu \ (1-\mu) \ \frac{d\sigma}{d\epsilon_s}} = M_1(4\gamma\epsilon) \ . \quad (23)$$

The integrals over μ and ϕ in Equation (23) have been performed by Jones (1968), with corrections given by Blumenthal & Gould (1970)[1] so that

$$M_1(x) = \frac{\int_0^{x/(1+x)} dy \ y \ J_C(x,y)}{\int_0^{x/(1+x)} dy \ J_C(x,y)} \quad (24)$$

where

$$J_C(x,y) = 2w \ln w + (1+2w)(1-w) + \frac{1}{2} \frac{(xw)^2}{1+xw}(1-w) \ , \quad (25)$$

in which

$$w = \frac{y}{x(1-y)} \ . \quad (26)$$

Analogous to $S_1(x)$, $M_1(x)$ is a function of only $x = 4\gamma\epsilon$, a useful property exploited by Moderski et al. (2005) and by myself in Section 2.4. It has the asymptotes

$$M_1(x) \rightarrow \begin{cases} x/3 & x \ll 1 \\ 0.6279 & x \gg 1 \end{cases} \ . \quad (27)$$

The function $M_1(x)$ and its asymptotes are plotted in Figure 5.

2.3. *Delta Function Scattering Approximation for General Seed Radiation Field*

Moderski et al. (2005) used a δ-function approximation for Compton scattering valid for isotropic seed photon fields and for point source seed photon fields. In

[1] An alternative but equivalent version of the result of this integration is given by Moderski et al. (2005).

this section I generalize this for a photon field with any angular distribution.

A δ-function approximation, valid for any seed photon field, is

$$\frac{d\sigma}{d\epsilon_s} \approx \sigma(\bar{\epsilon})\delta\left(\epsilon_s - \frac{5}{4}\langle\epsilon_s\rangle\right) \approx \sigma(\bar{\epsilon})\delta\left(\epsilon_s - \frac{5}{4}\gamma S_1(\bar{\epsilon})\right) \ . \quad (28)$$

The factor 5/4 comes from numerical experimentation, it leads to the best reproduction of the full calculation. The δ-function above can be rearranged so that

$$\frac{d\sigma}{d\epsilon_s} \approx \frac{4\langle\gamma\rangle}{5\epsilon_s}\sigma(\bar{\epsilon})S_2(\bar{\epsilon})\delta\left(\gamma - \langle\gamma\rangle\right) \quad (29)$$

where $\langle\gamma\rangle$ is obtained by solving

$$\frac{\epsilon_s}{\langle\gamma\rangle} = \frac{5}{4}S_1\left(\langle\gamma\rangle\epsilon(1-\cos\psi)\right) \ . \quad (30)$$

In general, Equation (30) must be solved numerically, for example using the routine `ZBRENT` from Press et al. (1992), although for the asymptotes given by Equation (22) it has the closed-form solutions

$$\langle\gamma\rangle \rightarrow \begin{cases} \sqrt{\frac{4\epsilon_s}{5\epsilon(1-\cos\psi)}} & x \ll 1 \\ \frac{4}{5}\epsilon_s & x \gg 1 \end{cases} \ . \quad (31)$$

Hereafter, in all calculations where the δ-approximation is used, I simplify the notation and allow $\langle\gamma\rangle \rightarrow \gamma$. In Equation (29),

$$S_2(x) = \frac{d\ln(x)}{d\ln(xS_1(x))} \ , \quad (32)$$

which has the asymptotes

$$S_2(x) \rightarrow \begin{cases} 1/2 & x \ll 1 \\ 1 & x \gg 1 \end{cases} \quad (33)$$

and is plotted in Figure 6. Putting the approximation Equation (29) in Equation (9) gives

$$\epsilon_s\, j(\epsilon_s,\Omega_s) \approx \frac{4}{5}\sigma_{\rm T}c\epsilon_s \int_0^{2\pi} d\phi \int_{-1}^{1} d\mu \times \int \frac{d\epsilon}{\epsilon^2} u(\epsilon,\Omega) n_e(\gamma,\Omega_s) \times S_3(\gamma\epsilon(1-\cos\psi)) \quad (34)$$

for $\gamma_{\rm min} < \gamma$, and

$$\epsilon_s\, j(\epsilon_s,\Omega_s) \approx \frac{4}{5}\sigma_{\rm T}c\epsilon_s \int_0^{2\pi} d\phi \int_{-1}^{1} d\mu \times \int \frac{d\epsilon}{\epsilon^2} u(\epsilon,\Omega) n_e(\gamma_{\rm min},\Omega_s) \times S_3(\gamma_{\rm min}\epsilon(1-\cos\psi)) \left(\frac{\gamma}{\gamma_{\rm min}}\right)^2 \quad (35)$$

for $\gamma < \gamma_{\rm min}$. Here

$$S_3(x) = xS_0(x)S_2(x) \ , \quad (36)$$

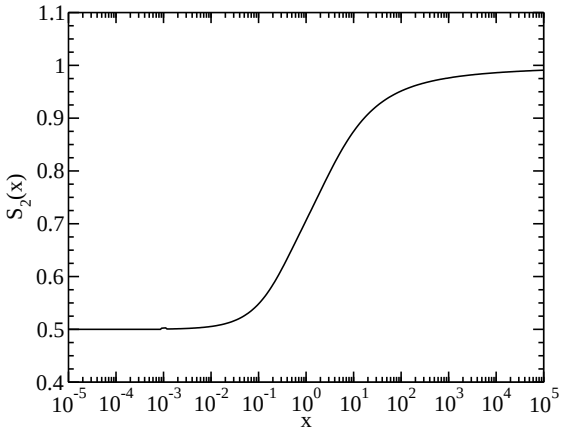

FIG. 6.— The function $S_2(x)$ given by Equation (32).

$$u(\epsilon,\Omega) = m_e c^2 \epsilon n_{ph}(\epsilon,\Omega) \ , \quad (37)$$

and

$$\gamma_{\rm min} = \frac{\epsilon_s}{2}\left[1 + \sqrt{1 + \frac{2}{\epsilon\epsilon_s(1-\cos\psi)}}\right] \ . \quad (38)$$

2.4. *Delta Function Scattering Approximation for Isotropic Seed Radiation Field*

In this section I derive the result for isotropic radiation fields, reproducing the result from Moderski et al. (2005).

For an isotropic seed photon field,

$$u(\epsilon,\Omega) = \frac{u(\epsilon)}{4\pi} \ , \quad (39)$$

the spherical symmetry implies that the result is independent of μ_s. Since one can then choose any value for μ_s, one can choose $\mu_s = 1$, so that

$$\epsilon_s\, j(\epsilon_s) = \frac{c\epsilon_s^2}{(4\pi)^2}\int_0^\infty \frac{d\epsilon}{\epsilon}\, u(\epsilon) \int_1^\infty d\gamma\ n_e(\gamma) \times \int_0^{2\pi} d\phi \int_{-1}^{1} d\mu\ (1-\mu)\ \frac{d\sigma}{d\epsilon_s} \ . \quad (40)$$

Here one can use the approximation

$$\int_0^{2\pi} d\phi \int_{-1}^{1} d\mu\ (1-\mu)\ \frac{d\sigma}{d\epsilon_s} \approx \int_0^{2\pi} d\phi \int_{-1}^{1} d\mu\ (1-\mu) \times \sigma_C(\gamma\epsilon(1-\mu))\delta\left(\epsilon_s - \frac{3}{2}\langle\epsilon_s\rangle_{\mu,\phi}\right) \approx \frac{3\pi\sigma_{\rm T}}{4\gamma^2\epsilon^2}M_0(4\gamma\epsilon)\delta\left(\epsilon_s - \frac{3}{2}\gamma M_1(4\gamma\epsilon)\right) \quad (41)$$

where the factor 3/2 comes from numerical experimentation.

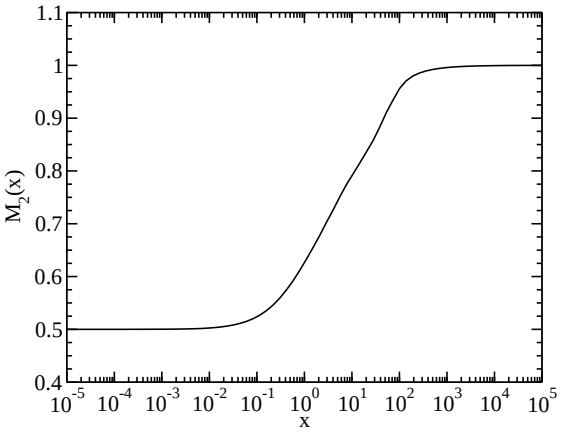

FIG. 7.— The function $M_2(x)$ given by Equation (45).

Substituting Equation (41) into Equation (40) and performing the integrals over μ, ϕ, and γ results in

$$\epsilon_s\, j(\epsilon_s) = \frac{c\sigma_{\rm T}\epsilon_s}{32\pi}\int_0^\infty \frac{d\epsilon}{\epsilon^3}\; u(\epsilon)\frac{n_e(\gamma)}{\gamma}M_3(4\gamma\epsilon) \qquad (42)$$

for $\gamma_{\rm min} < \gamma$, and

$$\epsilon_s\, j(\epsilon_s) = \frac{c\sigma_{\rm T}\epsilon_s}{32\pi}\int_0^\infty \frac{d\epsilon}{\epsilon^3}\; u(\epsilon)\frac{n_e(\gamma_{\rm min})}{\gamma_{\rm min}} \times M_3(4\gamma_{\rm min}\epsilon)\left(\frac{\gamma}{\gamma_{\rm min}}\right)^{3/2} \qquad (43)$$

for $\gamma < \gamma_{\rm min}$, where

$$M_3(x) = M_0(x)M_2(x)\ , \qquad (44)$$

$$M_2(x) = \frac{d\ln(x)}{d\ln(xM_1(x))}\ , \qquad (45)$$

and

$$\gamma_{\rm min} = \frac{\epsilon_s}{2}\left[1+\sqrt{1+\frac{1}{\epsilon\epsilon_s}}\right]\ . \qquad (46)$$

The function $M_2(x)$ has the asymptotes

$$M_2(x) \to \begin{cases} 1/2 & x \ll 1 \\ 1 & x \gg 1 \end{cases}\ . \qquad (47)$$

and is plotted in Figure 7. In general, one must solve

$$\frac{\epsilon_s}{\gamma} = \frac{3}{2}M_1(4\gamma\epsilon) \qquad (48)$$

for γ numerically. For the asymptotes given by Equation (27), Equation (48) can be solved analytically, so that

$$\gamma \to \begin{cases} \sqrt{\epsilon_s/(2\epsilon)} & x \ll 1 \\ \epsilon_s/(0.9419) & x \gg 1 \end{cases}\ . \qquad (49)$$

3. EXTERNAL COMPTON SCATTERING

Consider a homogeneous plasma "blob" moving at angle $\theta_s = \arccos\mu_s$ to our line of sight with relativistic speed βc relative to a stationary black hole and galaxy giving it a bulk Lorentz factor $\Gamma = (1-\beta^2)^{-1/2}$ and Doppler factor $\delta_{\rm D} = [\Gamma(1-\beta\mu_s)]^{-1}$. This represents a compact feature in a relativistic jet of a blazar. The blazar has cosmological redshift z giving it a luminosity distance $d_L(z)$. Quantities in the frame comoving with the blob are denoted by a prime, quantities in the "stationary" frame of the black hole and host galaxy are unmarked, and quantities in the observer frame are marked with an "obs". The observed νF_ν flux is

$$f_{\epsilon_s^{\rm obs}} = \frac{V_b\epsilon_s\, j(\epsilon_s,\Omega_s)}{d_L^2} \qquad (50)$$

where $\epsilon_s^{\rm obs} = \epsilon_s/(1+z)$, and V_b is the volume of the plasma blob in the stationary frame. The Compton-scattering of a stationary radiation field external to the blob can be calculated, following Georganopoulos et al. (2001) and Dermer et al. (2009), by transforming an isotropic comoving electron distribution to the stationary frame, so that

$$N_e(\gamma,\Omega_e) = \frac{\delta_{\rm D}^3 N_e'(\gamma/\delta_{\rm D})}{4\pi} \qquad (51)$$

where $N_e(\gamma,\Omega_e) = V_b n_e(\gamma,\Omega_e)$. Using this with Equations (34) and (35) for an arbitrary seed photon energy density one gets

$$f_{\epsilon_s^{\rm obs}} = \frac{c\sigma_{\rm T}\epsilon_s\delta_{\rm D}^3}{5\pi d_L^2}\int_0^{2\pi}d\phi\int_{-1}^1 d\mu \times\int_0^\infty\frac{d\epsilon}{\epsilon^2}u(\epsilon,\Omega)N_e'(\gamma/\delta_{\rm D}) \times S_3(\gamma\epsilon(1-\cos\psi)) \qquad (52)$$

for $\gamma_{\rm min} < \gamma$, and

$$f_{\epsilon_s^{\rm obs}} = \frac{c\sigma_{\rm T}\epsilon_s\delta_{\rm D}^3}{5\pi d_L^2}\int_0^{2\pi}d\phi\int_{-1}^1 d\mu \times\int_0^\infty\frac{d\epsilon}{\epsilon^2}u(\epsilon,\Omega)N_e'(\gamma_{\rm min}/\delta_{\rm D}) \times S_3(\gamma_{\rm min}\epsilon(1-\cos\psi))\left(\frac{\gamma}{\gamma_{\rm min}}\right)^2 \qquad (53)$$

for $\gamma < \gamma_{\rm min}$.

For an isotropic seed photon energy density, using Equations (42) and (43) one gets

$$f_{\epsilon_s^{\rm obs}} = \frac{c\sigma_{\rm T}\delta_{\rm D}^3\epsilon_s^{\rm obs}(1+z)}{32\pi d_L^2}\int_0^\infty\frac{d\epsilon}{\epsilon^3}u(\epsilon) \times\frac{N_e'(\gamma/\delta_{\rm D})}{\gamma}M_3(4\gamma\epsilon) \qquad (54)$$

for $\gamma_{\rm min} < \gamma$, and

$$f_{\epsilon_s^{\rm obs}} = \frac{c\sigma_{\rm T}\delta_{\rm D}^3\epsilon_s^{\rm obs}(1+z)}{32\pi d_L^2}\int_0^\infty\frac{d\epsilon}{\epsilon^3}u(\epsilon) \times\frac{N_e'(\gamma_{\rm min}/\delta_{\rm D})}{\gamma_{\rm min}}M_3(4\gamma_{\rm min}\epsilon)\left(\frac{\gamma}{\gamma_{\rm min}}\right)^{3/2} \qquad (55)$$

for $\gamma < \gamma_{\rm min}$.

3.1. *Isotropic Monochromatic Radiation Field*

External radiation fields such as the CMB, or those from the BLR, or dust torus, are often represented by an isotropic, monochromatic external radiation field. In this case,

$$u(\epsilon) = u_0 \delta(\epsilon - \epsilon_0) \ . \tag{56}$$

Using Equations (54) and (55) one gets

$$f_{\epsilon_s^{\rm obs}} = \frac{c\sigma_{\rm T}\delta_{\rm D}^3 \epsilon_s^{\rm obs}(1+z)}{32\pi d_L^2} \frac{u_0}{\epsilon_0^3} \times \frac{N_e'(\gamma/\delta_{\rm D})}{\gamma} M_3(4\gamma\epsilon_0) \tag{57}$$

for $\gamma_{\rm min} < \gamma$, and

$$f_{\epsilon_s^{\rm obs}} = \frac{c\sigma_{\rm T}\delta_{\rm D}^3 \epsilon_s^{\rm obs}(1+z)}{32\pi d_L^2} \frac{u_0}{\epsilon_0^3} \times \frac{N_e'(\gamma_{\rm min}/\delta_{\rm D})}{\gamma_{\rm min}} M_3(4\gamma_{\rm min}\epsilon_0) \left(\frac{\gamma}{\gamma_{\rm min}}\right)^{3/2} \tag{58}$$

for $\gamma < \gamma_{\rm min}$. In the Thomson regime, $4\gamma\epsilon_0 \ll 1$, Equation (57) reduces to

$$f_{\epsilon_s^{\rm obs}} \rightarrow \frac{\delta_{\rm D}^4}{6\pi d_L^2} c\sigma_{\rm T} \gamma_T^{'3} N_e'(\gamma_T') \ , \quad \gamma_T' = \frac{1}{\delta_{\rm D}} \sqrt{\frac{\epsilon_s^{\rm obs}(1+z)}{2\epsilon_0}} \ , \tag{59}$$

which is the approximation given in Equation (6.109) of Dermer & Menon (2009).

3.2. *Monochromatic Point Source Radially Behind Jet*

Scattering of photons from an accretion disk is sometimes approximated by the scattering of a monochromatic point source radially behind the jet; that is, at $\mu = 1$ (e.g., Dermer et al. 1992). In this case the external energy density is

$$u(\epsilon, \Omega) = \frac{L_0}{4\pi r^2 c} \frac{\delta(\mu - 1)}{2\pi} \delta(\epsilon - \epsilon_0) \ . \tag{60}$$

Then Equations (52) and (53) give

$$f_{\epsilon_s^{\rm obs}} = \frac{\epsilon_s L_0 \sigma_{\rm T} \delta_{\rm D}^3}{16\pi^2 r^2 d_L^2 \epsilon_0^2} S_3[\gamma\epsilon(1-\mu_s)] \times N_e'(\gamma/\delta_{\rm D}) \tag{61}$$

for $\gamma_{\rm min} < \gamma$, and

$$f_{\epsilon_s^{\rm obs}} = \frac{\epsilon_s L_0 \sigma_{\rm T} \delta_{\rm D}^3}{16\pi^2 r^2 d_L^2 \epsilon_0^2} S_3[\gamma_{\rm min}\epsilon(1-\mu_s)] \times N_e'(\gamma_{\rm min}/\delta_{\rm D}) \left(\frac{\gamma}{\gamma_{\rm min}}\right)^2 \tag{62}$$

for $\gamma < \gamma_{\rm min}$.

3.3. *Shakura-Sunyaev Accretion Disk*

The energy density of photons from an accretion disk from the solution of Shakura & Sunyaev (1973) can be approximated as

$$u(\epsilon) = \frac{3}{16\pi^2 c} \frac{\ell_{\rm Edd} L_{\rm Edd} R_g}{\eta R^3} \varphi(R) \delta(\epsilon - \epsilon_0(R)) \tag{63}$$

(Dermer & Schlickeiser 2002; Dermer et al. 2009) where

$$\epsilon_0(R) = 2.7 \times 10^{-4} \left(\frac{\ell_{\rm Edd}}{M_8 \eta}\right)^{1/4} \left(\frac{R}{R_g}\right)^{-3/4} \ , \tag{64}$$

$$R_g = \frac{GM}{c^2} \approx 1.5 \times 10^{13} M_8 \text{ cm} \ , \tag{65}$$

$$\varphi(R) = \sqrt{1 - \frac{R_{\rm in}}{R}} \ , \tag{66}$$

$\ell_{\rm Edd} = L_{\rm disk}/L_{\rm Edd}$, $L_{\rm disk}$ is the disk luminosity, $L_{\rm Edd} = 1.26 \times 10^{46} M_8$ is the Eddington luminosity, η is the accretion efficiency, $M_{\rm BH} = 10^8 M_8 M_\odot$ is the black hole mass, and $R_{\rm in}$ is the inner radius of the accretion disk. For a nonrotating Schwarzschild black hole, one expects that $R_{\rm in} = 6R_g$. For a rotating Kerr black hole, the inner radius is given by

$$R_{\rm in} = R_g \left\{ 3 + A_2 - \frac{|a|}{a} \left[(3 - A_1)(3 + A_1 + 2A_2)\right]^{1/2} \right\} \tag{67}$$

(e.g., Zhang et al. 1997) where

$$A_1 = 1 + (1-a^2)^{1/3} \times \left[(1+a)^{1/3} + (1-a)^{1/3}\right] \ , \tag{68}$$

$$A_2 = \sqrt{3a^2 + A_1^2} \ , \tag{69}$$

and a ($-1 \le a \le 1$) is the black hole spin.

The outer disk radius can be estimated as where the disk's self-gravity dominates over the black hole gravity (Laor & Netzer 1989; Netzer 2015). In this paper I simply use a constant value for the outer disk radius of $R_{\rm out} = 200 R_g$.

The Compton-scattered flux with the accretion disk as the seed photon source is, for $\gamma_{\rm min} < \gamma$,

$$f_{\epsilon_s^{\rm obs}} = \frac{3\epsilon_s \delta_{\rm D}^3 \ell_{\rm Edd} L_{\rm Edd} R_g \sigma_{\rm T}}{64\pi^3 d_L^2 \eta r^3} \int_0^{2\pi} d\phi \times \int_{\mu_{\rm min}}^{\mu_{\rm max}} d\mu \ \frac{\varphi(\mu)}{(\mu^{-2} - 1)^{3/2} \epsilon_0(\mu)^2} \times S_3[\gamma\epsilon_0(\mu)(1 - \cos\psi)] N_e'(\gamma/\delta_{\rm D}) \tag{70}$$

and, for $\gamma < \gamma_{\rm min}$,

$$f_{\epsilon_s^{\rm obs}} = \frac{3\epsilon_s \delta_{\rm D}^3 \ell_{\rm Edd} L_{\rm Edd} R_g \sigma_{\rm T}}{64\pi^3 d_L^2 \eta r^3} \int_0^{2\pi} d\phi \times \int_{\mu_{\rm min}}^{\mu_{\rm max}} d\mu \, \frac{\varphi(\mu)}{(\mu^{-2}-1)^{3/2}\epsilon_0(\mu)^2} \, , \times S_3[\gamma_{\rm min}\epsilon_0(\mu)(1-\cos\psi)] N'_e(\gamma_{\rm min}/\delta_{\rm D}) \times \left(\frac{\gamma}{\gamma_{\rm min}}\right)^2 \, , \quad (71)$$

where

$$\mu_{\rm min} = \frac{1}{\sqrt{1+(R_{\rm out}/r)^2}} \quad (72)$$

and

$$\mu_{\rm max} = \frac{1}{\sqrt{1+(R_{\rm in}/r)^2}} \, . \quad (73)$$

In Figure 8 I plot the Compton-scattered Shakura-Sunyaev accretion disk field, along with the Compton-scattered external isotropic monochromatic radiation field and the monochromatic point source from behind. The electron distribution used is a broken power-law, given by

$$N'_e(\gamma') = N_e(\gamma'_b) \begin{cases} (\gamma'/\gamma'_b)^{-p_1} & \gamma' \le \gamma'_b \\ (\gamma'/\gamma'_b)^{-p_2} & \gamma'_b < \gamma' \end{cases} \, . \quad (74)$$

The parameters for the "baseline" model for the comparison are given in Table 1; the parameter r is varied from the baseline model. In the monochromatic approximations, the seed photon energies are $\epsilon_0(R = 8.17R_g)$, as calculated from Equation (64). For the external isotropic radiation field calculation, the energy density of the scattered field (u_0) has been adjusted so that the normalization is approximately consistent with that of the scattered Shakura-Sunyaev disk field calculation. It is apparent that the isotropic monochromatic field is a poor approximation for the Shakura-Sunyaev disk field for scattering calculations. The monochromatic point source from behind is a reasonable approximation for the Shakura-Sunyaev disk field at large r.

3.4. *Reprocessing of Accretion Disk Radiation*

The accretion disk radiation described above can be absorbed and re-radiated as line emission in the broad-line region (BLR), or absorbed and re-radiated in the infrared as approximately a blackbody by a dust torus. The geometry for this setup is illustrated in Figure 9. Assuming that the disk radiation originates at the origin (the location of the central black hole), and that the re-processed emission is emitted isotropically so that it has emissivity $j_{\rm re}(\epsilon, \Omega_{\rm re}; R_{\rm re})$, then the energy density of the reprocessed emission is

$$u_{\rm re}(\epsilon) = \int dV_{\rm re} \frac{j_{\rm re}(\epsilon, \Omega_{\rm re}; R_{\rm re})}{4\pi x^2 c} \quad (75)$$

where $R_{\rm re}$ is the distance between the central source and the reprocessing medium, and x is the distance between the reprocessing medium and the emitting blob. Recall

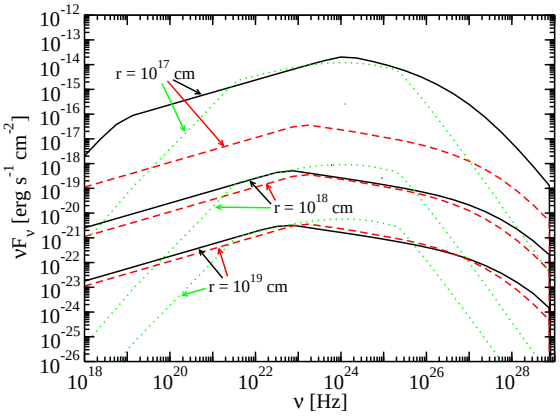

FIG. 8.— The SED of the Compton-scattered Shakura-Sunyaev accretion disk radiation (Equation [70] and [71]; solid black curves), the monochromatic point source behind the jet (Equation [57] and [58]; dashed red curves); and the external isotropic monochromatic radiation field (Equation [61] and [62]; dotted green curves) for various distances from the black hole r. The scattering of the external isotropic radiation field calculation had its energy density modified until its normalization approximately matched the scattered Shakura-Sunyaev calculation.

TABLE 1
PARAMETERS FOR NUMERICAL TESTS

Parameter	Symbol	Value
Lorentz factor	Γ	40
Doppler factor	$\delta_{\rm D}$	40
Magnetic Field [G]	B	0.56
ED[a] minimum Lorentz factor	γ'_1	20
ED[a] maximum Lorentz factor	γ'_2	5×10^7
ED[a] peak Lorentz factor	γ'_b	10^4
ED[a] first index	p_1	2
ED[a] second index	p_2	3.5
Black hole mass [$M_\odot$]	$M_{\rm BH}$	1.2×10^9
Gravitational radius [cm]	R_g	1.8×10^{14}
Disk luminosity [erg s^{-1}]	$L_{\rm disk}$	2×10^{46}
Accretion efficiency	η	1/12
Inner disk radius [R_g]	$R_{\rm in}$	6
Outer disk radius [R_g]	$R_{\rm out}$	200
BL[b] dimensionless energy	$\epsilon_{\rm li}$	2×10^{-5}
BL[b] scattering fraction	$\xi_{\rm li}$	0.024
BL[b] radius [cm]	$R_{\rm li}$	10^{17}
DT Temperature	$\epsilon_{\rm dt}$	10^3
DT[b] scattering fraction	$\xi_{\rm dt}$	0.1
DT[b] inner radius [cm]	$R_{\rm dt,1}$	1.6×10^{19}
DT[b] outer radius [cm]	$R_{\rm dt,2}$	1.6×10^{20}
DT[b] gradient	ζ	1.0
blob distance from black hole [cm]	r	10^{17}

[a] Electron Distribution
[b] Broad Line
[c] Dust Torus

that r is the distance between central source and the emitting blob, so that

$$x^2 = R_{\rm re}^2 + r^2 - 2rR_{\rm re}\mu_{\rm re} \, . \quad (76)$$

The energy density per solid angle [where $u(\epsilon) = \int d\Omega \; u(\epsilon, \Omega)$] can be found by imposing δ-function con-

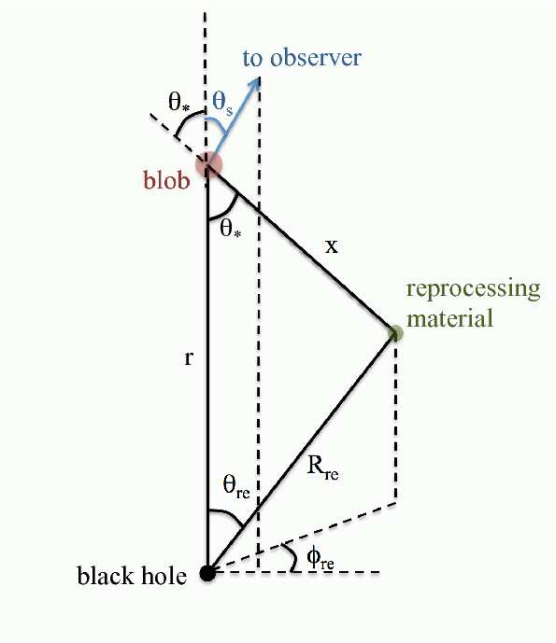

FIG. 9.— An illustration of the geometry of reprocessed emission as a seed photon source for Compton scattering by electrons in the blob.

straints (Böttcher & Dermer 1995; Dermer et al. 2009),

$$u_{\rm re}(\epsilon,\Omega) = \int dV_{\rm re} \frac{j_{\rm re}(\epsilon,\Omega_{\rm re};R_{\rm re})}{4\pi x^2 c} \times \delta(\phi-\phi_{\rm re})\delta(\mu-\mu_*) = \frac{1}{4\pi c}\int_0^{2\pi} d\phi_{\rm re}\int_{-1}^{1} d\mu_{\rm re}\int_0^{\infty} dR_{\rm re} \times \left(\frac{R_{\rm re}}{x}\right)^2 j_{\rm re}(\epsilon,\Omega_{\rm re};R_{\rm re}) \times \delta(\phi-\phi_{\rm re})\delta(\mu-\mu_*) \quad (77)$$

where

$$\mu_*^2 = 1-\left(\frac{R_{\rm re}}{x}\right)^2(1-\mu_{\rm re}^2)\ . \quad (78)$$

3.5. *Broad Line Region*

The BLR around black holes reprocesses disk radiation into line emission that is Doppler-broadened by the BLR clouds' orbits around the black hole. Reverberation mapping indicates that individual lines emit primarily in a relatively narrow distance from the black hole, and that different lines are emitted at different radii (e.g., Peterson & Wandel 1999; Kollatschny 2003; Peterson et al. 2014). Thus it seems reasonable to assume, at least for the purposes of Compton scattering, that each line is monochromatic, emitting photons with dimensionless energy $\epsilon_{\rm li}$ (i.e., ignoring the Doppler-broadening of the line) and emitted at one distance from the BLR with radius $R_{\rm li}$. I consider two possible geometries for the BLR, a spherical shell and a flattened annulus. A simple empirical model for estimating the luminosities (equivalently, $\xi_{\rm li}$) and radii ($R_{\rm li}$) of broad lines is presented in Appendix A.

3.5.1. *Spherical Shell Broad Line Region*

I consider here that each line is emitted from an infinitesimally thin spherical shell with radius $R_{\rm li}$ from the origin and monochromatic dimensionless energy $\epsilon_{\rm li}$. In this case the emissivity of the radiation from a single line is

$$j_{\rm re}(\epsilon,\Omega_{\rm re};R_{\rm li}) = \frac{\xi_{\rm li}L_{\rm disk}}{4\pi R_{\rm li}^2}\delta(\epsilon-\epsilon_{\rm li})\delta(R_{\rm re}-R_{\rm li}) \quad (79)$$

where $\xi_{\rm li}$ is the fraction of disk radiation reprocessed by the line. Using this in Equation (77) gives

$$u_{\rm re}(\epsilon,\Omega) = \frac{\xi_{\rm li}L_{\rm disk}}{(4\pi)^2 c}\delta(\epsilon-\epsilon_{\rm li})\int_{-1}^{1}\frac{d\mu_{\rm re}}{x^2}\ \delta(\mu-\mu_*) \quad (80)$$

for the line energy density. The observed flux from Compton scattering BLR photons is then

$$f_{\epsilon_s^{\rm obs}} = \frac{\xi_{\rm li}L_{\rm disk}\sigma_{\rm T}\delta_{\rm D}^3}{80\pi^3 d_L^2}\left(\frac{\epsilon_s}{\epsilon_{\rm li}^2}\right)\int_0^{2\pi}d\phi \times\int_{-1}^{1}\frac{d\mu_{\rm re}}{x^2}S_3[\gamma\epsilon_0(1-\cos\bar{\psi})]N_e'(\gamma/\delta_{\rm D}) \quad (81)$$

for $\gamma_{\rm min}<\gamma$ and

$$f_{\epsilon_s^{\rm obs}} = \frac{\xi_{\rm li}L_{\rm disk}\sigma_{\rm T}\delta_{\rm D}^3}{80\pi^3 d_L^2}\left(\frac{\epsilon_s}{\epsilon_{\rm li}^2}\right)\int_0^{2\pi}d\phi \times\int_{-1}^{1}\frac{d\mu_{\rm re}}{x^2}S_3[\gamma_{\rm min}\epsilon_0(1-\cos\bar{\psi})] \times N_e'(\gamma_{\rm min}/\delta_{\rm D})\left(\frac{\gamma}{\gamma_{\rm min}}\right)^2 \quad (82)$$

for $\gamma<\gamma_{\rm min}$ where

$$\cos\bar{\psi} = \mu_*\mu_s + \sqrt{1-\mu_*^2}\sqrt{1-\mu_s^2}\cos\phi\ . \quad (83)$$

3.5.2. *Flattened Broad Line Region*

There is some evidence that the BLR is not a spherical shell, but flatted (e.g., McLure & Dunlop 2001; Decarli et al. 2011; Shaw et al. 2012). Thus I also consider a model for the BLR where each line emits in an infinitesimally thin ring with radius $R_{\rm li}$ oriented orthogonal to the jet axis. This can be computed by considering an additional δ-function constraint on $\mu_{\rm re}$, so that the emissivity of a line is

$$j_{\rm re}(\epsilon,\Omega_{\rm re};R_{\rm li}) = \frac{\xi_{\rm li}L_{\rm disk}}{4\pi R_{\rm li}^2}\delta(R_{\rm re}-R_{\rm li}) \times\delta(\epsilon-\epsilon_{\rm li})\ \delta(\mu_{\rm re}-0)\ . \quad (84)$$

Using Equation (84) in Equation (77) gives

$$u_{\rm re}(\epsilon,\Omega) = \frac{\xi_{\rm li}L_{\rm disk}}{(4\pi)^2 c x^2}\delta(\mu-r/x)\delta(\epsilon-\epsilon_{\rm li}) \quad (85)$$

for the energy density, where

$$x^2 = R_{\rm li}^2 + r^2\ . \quad (86)$$

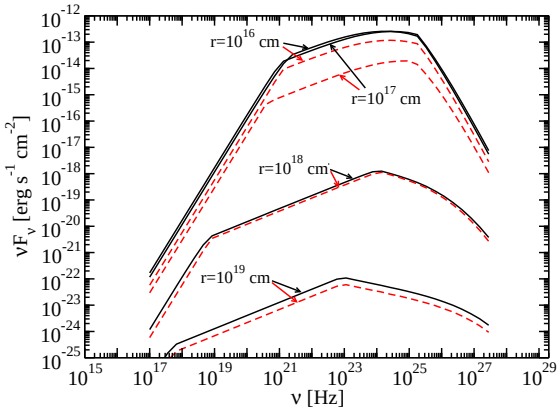

FIG. 10.— The SED of the Compton-scattered BLR radiation for a shell geometry (Equation [81] and [82]; solid black curves), and for a flattened geometry (Equation [87] and [88]; dashed red curves) for various distances r from the black hole.

The observed flux from Compton-scattering this radiation field is

$$f_{\epsilon_s^{\rm obs}} = \frac{\epsilon_s \xi_{\rm li} L_{\rm disk} \sigma_{\rm T} \delta_{\rm D}^3}{80\pi^3\ x^2 d_L^2 \epsilon_{\rm li}^2} \int_0^{2\pi} d\phi \times S_3[\gamma\epsilon(1-\cos\bar{\psi})] N'_e(\gamma/\delta_{\rm D}) \quad (87)$$

for $\gamma_{\rm min} < \gamma$, and

$$f_{\epsilon_s^{\rm obs}} = \frac{\epsilon_s \xi_{\rm li} L_{\rm disk} \sigma_{\rm T} \delta_{\rm D}^3}{80\pi^3\ x^2 d_L^2 \epsilon_{\rm li}^2} \times \int_0^{2\pi} d\phi\ S_3[\gamma_{\rm min}\epsilon(1-\cos\bar{\psi})] \times N'_e(\gamma_{\rm min}/\delta_{\rm D}) \left(\frac{\gamma}{\gamma_{\rm min}}\right)^2 \quad (88)$$

for $\gamma < \gamma_{\rm min}$, where

$$\cos\bar{\psi} = \frac{r\mu_s}{x} + \sqrt{1-\frac{r^2}{x^2}}\sqrt{1-\mu_s^2}\cos\phi\ . \quad (89)$$

In Figure 10 I plot the Compton-scattered BLR radiation field for both the shell and flattened BLR geometry. I use the same parameters as in Table 1, while varying the distance of the emitting region from the black hole (r). In general, the flattened geometry gives a slightly lower flux compared to the shell geometry. This is most apparent at the distance of the BLR line radius, $r = R_{\rm li} = 10^{17}$ cm.

3.6. *Dust Torus*

Dust tori found in AGN emit approximately as blackbodies and are thought to be oriented orthogonal to the jet axes, although its exact geometry is uncertain. Here I will use two approximations for the dust torus, useful for Compton-scattering. In both cases I will approximate the dust torus blackbody as monochromatic with energy at the peak of the blackbody distribution, $\epsilon = 2.7\Theta$, where $\Theta = kT_{\rm dt}/(m_e c^2)$ is the dimensionless temperature of the dust torus. To avoid sublimation, the dust torus temperature $T_{\rm dt} \lesssim 2000$ K. One could modify the expressions below to use the full blackbody expression by allowing

$$\delta(\epsilon - 2.7\Theta) \rightarrow \frac{15}{\pi^4\Theta^4}\frac{\epsilon^3}{e^{\epsilon/\Theta}-1}\ .$$

3.6.1. *Ring Dust Torus*

Here I approximate the dust torus as an infinitesimally thin annulus with radius $R_{\rm dt}$. This is essentially the same approximation as the ring BLR (Section 3.5.2). For this case the emissivity is

$$j_{\rm re}(\epsilon,\Omega;R_{\rm dt}) = \frac{\xi_{\rm dt}L_{\rm disk}}{4\pi R_{\rm re}^2}\delta(R_{\rm re}-R_{\rm dt}) \times \delta(\epsilon-2.7\Theta)\ \delta(\mu_{\rm re}-0)\ . \quad (90)$$

Using this in Equation (77) gives

$$u_{\rm re}(\epsilon,\Omega) = \frac{\xi_{\rm dt}L_{\rm disk}}{(4\pi)^2 c x^2}\delta(\mu - r/x)\delta(\epsilon-2.7\Theta) \quad (91)$$

for the dust torus energy density, where

$$x^2 = R_{\rm dt}^2 + r^2\ . \quad (92)$$

The observed flux from Compton-scattering this radiation field is

$$f_{\epsilon_s^{\rm obs}} = \frac{\epsilon_s \xi_{\rm dt} L_{\rm disk} \sigma_{\rm T} \delta_{\rm D}^3}{80\pi^3 (2.7\Theta)^2 x^2 d_L^2} \int_0^{2\pi} d\phi \times S_3[2.7\gamma\Theta(1-\cos\bar{\psi})] N'_e(\gamma/\delta_{\rm D}) \quad (93)$$

for $\gamma_{\rm min} < \gamma$, and

$$f_{\epsilon_s^{\rm obs}} = \frac{\epsilon_s \xi_{\rm dt} L_{\rm disk} \sigma_{\rm T} \delta_{\rm D}^3}{80\pi^3 (2.7\Theta)^2 x^2 d_L^2} \int_0^{2\pi} d\phi \times S_3[2.7\gamma_{\rm min}\Theta(1-\cos\bar{\psi})] \times N'_e(\gamma_{\rm min}/\delta_{\rm D}) \left(\frac{\gamma}{\gamma_{\rm min}}\right)^2 \quad (94)$$

for $\gamma < \gamma_{\rm min}$, where

$$\cos\bar{\psi} = \frac{r\mu_s}{x} + \sqrt{1-\frac{r^2}{x^2}}\sqrt{1-\mu_s^2}\cos\phi\ . \quad (95)$$

The dust torus radius can be estimated as the sublimation radius,

$$R_{\rm dt} = 3.5\times10^{18}\left(\frac{L_{\rm disk}}{10^{45}\ {\rm erg\ s^{-1}}}\right)^{1/2} \times \left(\frac{T_{\rm dt}}{10^3\ {\rm K}}\right)^{-2.6}\ {\rm cm} = 8\times10^5\left(\frac{\ell_{\rm Edd}}{M_8}\right)^{1/2} T_{\rm dt,3}^{-2.6}\ R_g \quad (96)$$

(Nenkova et al. 2008b; Sikora et al. 2009) where $T_{\rm dt,3} = T_{\rm dt}/(10^3\ {\rm K})$.

3.6.2. *Extended Dust Torus*

I have created another approximation to the dust torus based on the dust modeling of Nenkova et al. (2008a,b). I approximate the dust torus as as a flattened disk with inner and outer radii, $R_{\rm dt,1}$ and $R_{\rm dt,2}$, respectively. The dust torus consists of a number of dust clouds, each with cross sectional area $\Sigma_{\rm cl}$. The dust cloud number density scales as a power-law with distance from the black hole (R), so that it is

$$n_{\rm cl}(R) = n_{\rm cl,0}\left(\frac{R}{R_{\rm dt,1}}\right)^{-\zeta} H(R;R_{\rm dt,1},R_{\rm dt,2})\ . \quad (97)$$

Other parameters of the dust torus ($\Sigma_{\rm cl}$ and Θ) do not vary with R in my model, although in principle they could. The fraction of disk luminosity reprocessed by this dust torus is

$$\xi_{\rm dt} = \int_0^\infty dR\ \Sigma_{\rm cl}\ n_{\rm cl}(R) = \Sigma_{\rm cl} n_{\rm cl,0} R_{\rm dt,eff} \tag{98}$$

where

$$R_{\rm dt,eff} = \begin{cases} [R_{\rm dt,1} - R_{\rm dt,2}(R_{\rm dt,2}/R_{\rm dt,1})^{-\zeta}]/(\zeta - 1) & \zeta \neq 1 \\ R_{\rm dt,1} \ln(R_{\rm dt,2}/R_{\rm dt,1}) & \zeta = 1 \end{cases} . \tag{99}$$

With this formulation, the reprocessed emissivity is

$$\begin{aligned} j_{\rm re}(\epsilon, \Omega; R_{\rm re}) &= \frac{L_{\rm disk}}{4\pi R_{\rm re}^2} \Sigma_{\rm cl} n_{\rm cl}(R_{\rm re}) \\ &\times \delta(\epsilon - 2.7\Theta)\ \delta(\mu_{\rm re} - 0) \\ &= \frac{\xi_{\rm dt} L_{\rm disk}}{4\pi R_{\rm re}^2} \frac{\delta(\epsilon - 2.7\Theta)\ \delta(\mu_{\rm re} - 0)}{R_{\rm dt,eff}} , \end{aligned} \tag{100}$$

and Equation (77) gives

$$\begin{aligned} u_{\rm re}(\epsilon, \Omega) &= \frac{\xi_{\rm dt} L_{\rm disk} \delta(\epsilon - 2.7\Theta)}{(4\pi)^2 c R_{\rm dt,eff}} \int_{R_{\rm dt,1}}^{R_{\rm dt,2}} \frac{dR_{\rm re}}{x^2} \\ &\times \left(\frac{R_{\rm re}}{R_{\rm dt,1}}\right)^{-\zeta} \delta(\mu - r/x) \end{aligned} \tag{101}$$

where

$$x^2 = R_{\rm re}^2 + r^2 . \tag{102}$$

The observed Compton-scattered flux is then

$$\begin{aligned} f_{\epsilon_s^{\rm obs}} &= \frac{\epsilon_s \xi_{\rm dt} L_{\rm disk} \sigma_{\rm T} \delta_{\rm D}^3}{80\pi^3 (2.7\Theta)^2 d_L^2 R_{\rm dt,eff}} \int_0^{2\pi} d\phi \\ &\times \int_{R_{\rm dt,1}}^{R_{\rm dt,2}} \frac{dR_{\rm re}}{x^2} \left(\frac{R}{R_{\rm dt,1}}\right)^{-\zeta} \\ &\times S_3[2.7\gamma\Theta(1 - \cos\bar{\psi})] N_e'(\gamma/\delta_{\rm D}) \end{aligned} \tag{103}$$

for $\gamma_{\rm min} < \gamma$, and

$$\begin{aligned} f_{\epsilon_s^{\rm obs}} &= \frac{\epsilon_s \xi_{\rm dt} L_{\rm disk} \sigma_{\rm T} \delta_{\rm D}^3}{80\pi^3 (2.7\Theta)^2 d_L^2 R_{\rm dt,eff}} \int_0^{2\pi} d\phi \\ &\times \int_{R_{\rm dt,1}}^{R_{\rm dt,2}} \frac{dR_{\rm re}}{x^2} \left(\frac{R}{R_{\rm dt,1}}\right)^{-\zeta} \\ &\times S_3[2.7\gamma_{\rm min}\Theta(1 - \cos\bar{\psi})] \\ &\times N_e'(\gamma_{\rm min}/\delta_{\rm D}) \left(\frac{\gamma}{\gamma_{\rm min}}\right)^2 \end{aligned} \tag{104}$$

for $\gamma < \gamma_{\rm min}$. Modeling by Nenkova et al. (2008b) indicated that $R_{\rm dt,2}/R_{\rm dt,1} = 5 - 10$ and $\zeta = 1 - 2$ with the inner dust radius $R_{\rm dt,1}$ constrained by Equation (96). A similar dust torus model to this one was used for Compton scattering calculations by Sikora et al. (2013).

In Figure 11 I plot the Compton-scattered dust radiation field for the ring and extended dust torus models. I use the parameters in Table 1, with the distance of the emitting region from the black hole (r) varying. At smaller r, the ring model gives a greater Compton-scattered flux. However, for $r > R_{\rm dt,1}$ the extended dust torus model gives greater flux, since in the extended model there are more infrared photons at larger radii available for scattering.

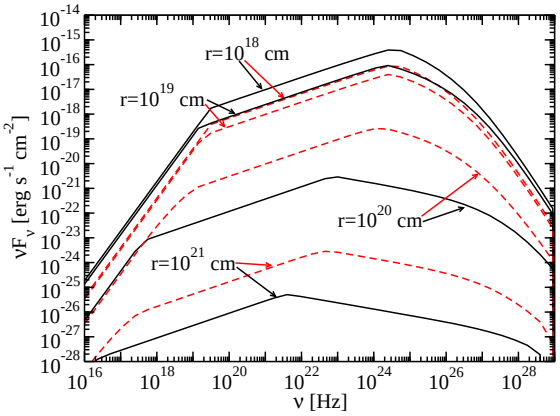

FIG. 11.— The SED of the Compton-scattered dust torus radiation for a ring geometry (Equation [93] and [94]; solid black curves), and for an extended torus geometry (Equation [103] and [104]; dashed red curves) for various distances r from the black hole.

4. SYNCHROTRON SELF-COMPTON

The observed νF_ν flux from a spherical plasma blob can be written in terms of a spherically-symmetric comoving emissivity,

$$f_{\epsilon_s^{\rm obs}} = \frac{\delta_{\rm D}^4 V_b' \epsilon_s' j'(\epsilon_s')}{4\pi d_L^2} . \tag{105}$$

The comoving synchrotron energy density in a spherical blob is

$$u'(\epsilon') = \frac{3 d_L^2 (1+z)^2 f_\epsilon^{sy}}{c^3 t_{\rm v,min}^2 \delta_{\rm D}^6 \epsilon'} \tag{106}$$

where

$$t_{\rm v,min} = \frac{(1+z) R_b'}{\delta_{\rm D} c} \tag{107}$$

and R_b' is the comoving blob radius (Finke et al. 2008). The observed flux from Compton-scattering this radiation field, known as synchrotron self-Compton (SSC), can be written, using the δ approximation from Section 2.4, as

$$\begin{aligned} f_{\epsilon_s^{\rm obs}} &= \frac{3\sigma_{\rm T} \epsilon_s^{\rm obs}}{32\pi c^2 t_{\rm v,min}^2 \delta_{\rm D}^2} \int_0^\infty d\epsilon' \frac{f_\epsilon^{sy}}{\epsilon'^4} \\ &\times \frac{N_e'(\gamma')}{\gamma'} M_3(4\gamma'\epsilon') \end{aligned} \tag{108}$$

for $\gamma_{\rm min}' < \gamma'$, and

$$\begin{aligned} f_{\epsilon_s^{\rm obs}} &= \frac{3\sigma_{\rm T} \epsilon_s^{\rm obs}}{32\pi c^2 t_{\rm v,min}^2 \delta_{\rm D}^2} \int_0^\infty d\epsilon' \frac{f_\epsilon^{sy}}{\epsilon'^4} \\ &\times \frac{N_e'(\gamma_{\rm min}')}{\gamma_{\rm min}'} M_3(2\gamma_{\rm min}'\epsilon') \left(\frac{\gamma'}{\gamma_{\rm min}'}\right)^{3/2} \end{aligned} \tag{109}$$

for $\gamma' < \gamma_{\rm min}'$. The synchrotron flux f_ϵ^{sy} can be computed as described by, for example, Finke et al. (2008).

TABLE 2
Speed factor improvement of delta approximation.

Seed Radiation Field	Equation	Speed Improvement
Isotropic Monochromatic	Equation (56)	3
Point Source Behind Jet	Equation (60)	1.5
Accretion Disk	Equation (63)	26
Broad Line Region (shell)	Equation (80)	11
Broad Line Region (ring)	Equation (85)	8
Dust torus (ring)	Equation (91)	8
Dust torus (extended)	Equation (101)	24
Synchrotron	Equation (106)	6

5. NUMERICAL RESULTS

The approximations using the δ-function approximation given in the previous sections can significantly speed up Compton-scattering calculations. It is possible to store the functions $S_0(x)$, $S_1(x)$, etc. in a data table that is read in at the beginning of the program, which allows them to be calculated very quickly. This essentially eliminates the need to do one of the integrals numerically. I have compared calculations using the exact expressions from, for example, Finke et al. (2008) and Dermer et al. (2009), with results using the δ-function approximation, described in Sections 3 and 4. I present some of those comparisons here. As in Sections 3.3, 3.5, and 3.6, I use the baseline model parameters in Table 1. In the figures I vary parameters from this baseline model.

In the left panel of Figure 12 I compare Compton scattering of disk photons, as described in Section 3.3. Values of p_2 were varied. The right panel of Figure 12 shows a comparison of scattering of broad line photons, as described in Section 3.5. In most cases the approximation is better than 5%, although it is higher near the endpoints or near the frequency associated with $\gamma' = \gamma'_b$, where it can be as high as 12%.

I also tested the speed of the δ approximation and compared it to the full integral calculation. The exact improvement depends on many factors, such as the computer used and the numerical integration technique. A full exploration of these factors is beyond the scope of this paper, and not particularly interesting. For the calculations I performed, with integrations done by the simple trapezoid rule, the factor of the speed improvement of the δ approximation is given in Table 2. The speed-up is considerable, greater than a factor of 10 in many cases. Generally the more integrals a calculation requires, the faster the improvement in speed.

6. BEAMING PATTERN

It is tempting to think that population studies (e.g., Gardner & Done 2014) of FSRQs might be able to distinguish between different geometries for the external scattered photon field. One can use the results in the previous sections to derive the beaming pattern of the flux density in the Thomson regime for external Compton scattering. This assume a power-law electron distribution, $N'_e(\gamma') \propto \gamma'^{-p}$.

For an isotropic monochromatic external radiation field, Section 3.1, the flux density goes as

$$F_\nu \propto \nu^{-\alpha}\ \delta_{\rm D}^{4+2\alpha} \tag{110}$$

where $\nu = \epsilon_{obs} m_e c^2/h$, $h = 6.626\times10^{-27}$ erg s is Planck's constant, and $\alpha = (p-1)/2$. Equation (110) was found previously by Georganopoulos et al. (2001).

For a point source radially behind the jet, Section 3.2,

$$F_\nu \propto \frac{\nu^{-\alpha}}{r^2}\ \delta_{\rm D}^{4+2\alpha}\ (1-\mu_s)^{1+\alpha}\ , \tag{111}$$

which was found previously by Dermer (1995). For a shell BLR, Section 3.5.1,

$$F_\nu \propto \nu^{-\alpha}\ \delta_{\rm D}^{4+2\alpha} \int_0^{2\pi} d\phi_*\ \int_{-1}^{1} \frac{d\mu_{\rm re}}{x^2} \times (1-\cos\bar{\psi})^{1+\alpha}\ , \tag{112}$$

where

$$\cos\bar{\psi} = \mu_*\mu_s + \sqrt{1-\mu_*^2}\sqrt{1-\mu_s^2}\cos\phi_*\ , \tag{113}$$

$$x^2 = R_{\rm re}^2 + r^2 - 2rR_{\rm re}\mu_{\rm re}\ , \tag{114}$$

and

$$\mu_*^2 = 1 - \left(\frac{R_{\rm re}}{x}\right)^2 (1-\mu_{\rm re}^2)\ . \tag{115}$$

For a ring BLR or ring dust torus, Sections 3.5.2 and 3.6,

$$F_\nu \propto \frac{\nu^{-\alpha}}{x^2}\ \delta_{\rm D}^{4+2\alpha}\ \int_0^{2\pi} d\phi_*\ (1-\cos\bar{\psi})^{1+\alpha}\ , \tag{116}$$

where now

$$\cos\bar{\psi} = \mu_s\frac{r}{x} + \sqrt{1-\mu_s^2}\sqrt{1-\left(\frac{r}{x}\right)^2}\cos\phi_* \tag{117}$$

and $x^2 = R_{\rm re}^2 + r^2$.

For $r \ll R_{\rm re}$ and $r \gg R_{\rm re}$, both the spherical shell and ring reduce to the isotropic case and point source case, respectively. This is demonstrated in Figure 13. The ring case is actually a small amount brighter at small angles than the spherical shell for the case where $r = 10R_{\rm li}$. When the emitting region is at this distance, more of the photons from the ring are at a favorable geometry for efficient Compton scattering compared to the spherical shell. However, there is little difference between the beaming pattern for these different external radiation field geometries. It is unlikely that beaming pattern studies could distinguish between them.

7. PHOTOABSORPTION

The same radiation fields that are Compton-scattered to produce γ rays can also absorb the γ rays to produce electron-positron pairs. The γ-ray spectrum is attenuated by a factor $e^{-\tau_{\gamma\gamma}(\epsilon_1)}$ where the absorption optical depth for this process is

$$\tau_{\gamma\gamma}(\epsilon_1) = \int_r^\infty d\ell \int_0^{2\pi} d\phi \int_{-1}^{1} d\mu \times (1-\cos\psi)\int_0^\infty d\epsilon\ \frac{u(\epsilon,\Omega;\ell)}{\epsilon m_e c^2} \times \sigma_{\gamma\gamma}\left[\frac{\epsilon\epsilon_1(1+z)}{2}(1-\cos\psi)\right]\ , \tag{118}$$

(e.g., Dermer et al. 2009), where ψ is the angle between the two incoming photons, the $\gamma\gamma$ polarization-averaged

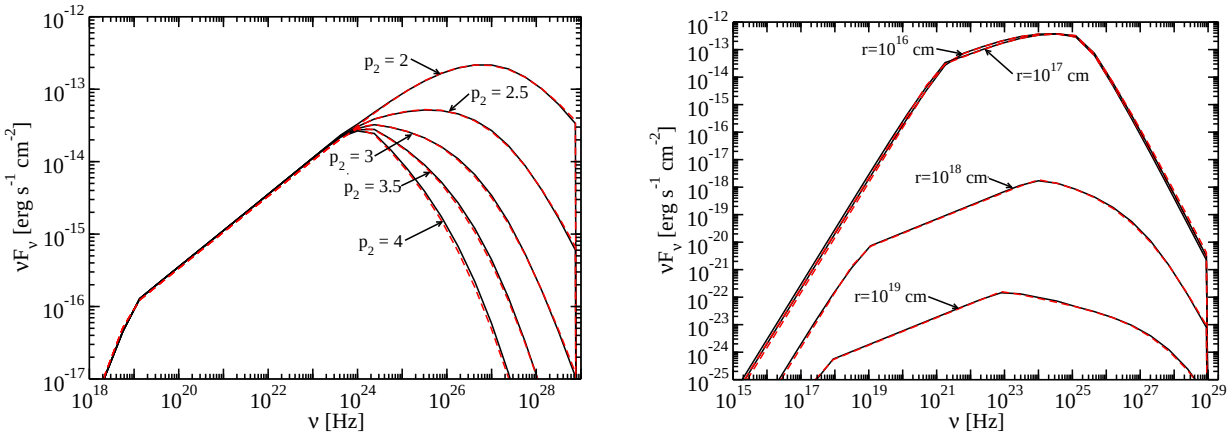

FIG. 12.— Comparison of exact and δ-function Compton-scattering calculations. The solid black curve is the exact expression, the dashed red curve is the δ-function approximation. *Left*: The scattering of disk photons for different values of p_2, as indicated on the plot. *Right*: The scattering of Lyα BLR photons assuming a shell geometry for different distances from the black hole (r), as indicated on the plot.

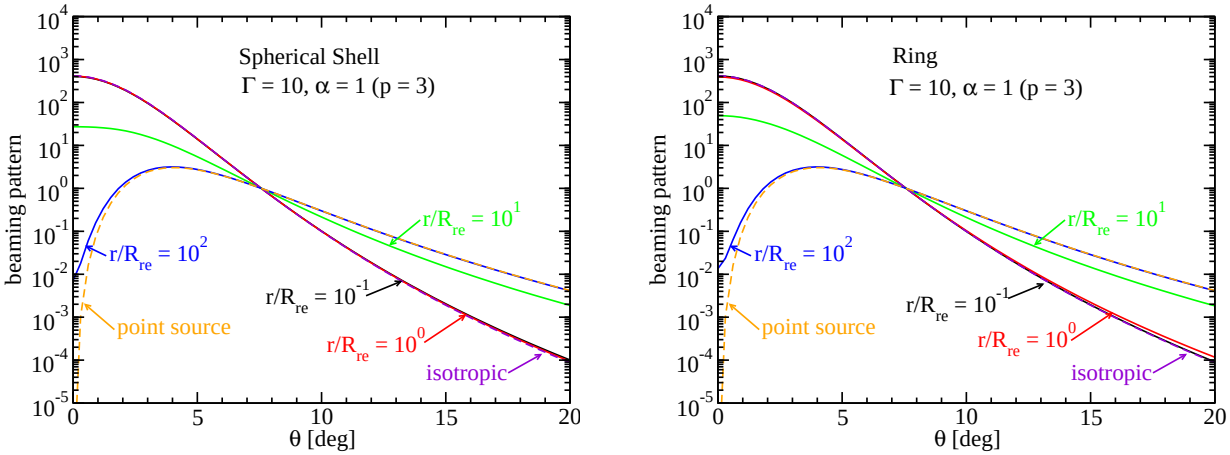

FIG. 13.— The beaming pattern for various external radiation field geometries, normalized at $\theta = 7.5°$, for $\Gamma = 10$ and $p = 3$. The isotropic and point source cased are shown as the violet and orange dashed curves, respectively. The exact cases at various values of $r/R_{\rm re}$ are shown as the solid curves, as indicated. *Left*: a spherical shell external radiation field (Section 3.5.1). *Right*: a ring external radiation field (Section 3.5.2).

absorption cross-section is

$$\sigma_{\gamma\gamma}(s) = \frac{3}{8}\sigma_{\rm T}(1-\beta_{\rm cm}^2) \times\left[(3-\beta_{\rm cm}^4)\ln\left(\frac{1+\beta_{\rm cm}}{1-\beta_{\rm cm}}\right) - 2\beta_{\rm cm}(2-\beta_{\rm cm}^2)\right], \quad (119)$$

and

$$\beta_{\rm cm} = \sqrt{1-s^{-1}} \quad (120)$$

(e.g., Gould & Schréder 1967; Brown et al. 1973; Jauch & Rohrlich 1976; Böttcher 2014). I use these equations below to find expressions for $\tau_{\gamma\gamma}$ by various external radiation fields. In so doing I assume the γ-ray photons are traveling directly along the jet axis, i.e., $\mu_s = 1$, so that $\cos\psi \to \mu$.

7.1. *Absorption by Accretion Disk Photons*

For absorption of γ rays by accretion disk photons, using Equation (63),

$$\tau_{\gamma\gamma}(\epsilon_1) = 10^7\,\frac{\ell_{\rm Edd}^{3/4}M_8^{1/4}}{\eta^{3/4}}\int_{\tilde r}^{\infty}\frac{d\tilde\ell}{\tilde\ell^2} \times\int_{\tilde R_{\rm in}}^{\tilde R_{\rm out}}\frac{d\tilde R}{\tilde R^{5/4}}\,\frac{\phi(\tilde R)}{(1+\tilde R^2/\tilde\ell^2)^{3/2}} \times\left[\frac{\sigma_{\gamma\gamma}(\tilde s)}{\sigma_{\rm T}}\right](1-\mu) \quad (121)$$

where $\tilde R = R/R_g$, $\tilde r = r/R_g$, $\tilde\ell = \ell/R_g$,

$$\tilde s = \frac{\epsilon_0(\tilde R)\epsilon_1(1+z)(1-\mu)}{2}\,, \quad (122)$$

and $\mu = (1+\tilde R^2/\tilde\ell^2)^{-1/2}$. This result was found by Dermer et al. (2009). Similar calculations

of $\gamma\gamma$ absorption by disk photons have been done by Becker & Kafatos (1995) and Donea & Protheroe (2003).

7.2. *Absorption by Broad Line Region Photons*

For absorption of γ rays by photons from a broad-line shell, Equation (80),

$$\tau_{\gamma\gamma}(\epsilon_1) = 900\ \frac{\xi_{\rm li}\ell_{\rm Edd}}{\epsilon_{\rm li}} \int_{\tilde{r}}^{\infty} d\tilde{\ell} \times \int_{-1}^{1} \frac{d\mu_{\rm re}}{\tilde{x}^2} \left[\frac{\sigma_{\gamma\gamma}(\tilde{s})}{\sigma_{\rm T}}\right] (1-\mu_*) \quad (123)$$

where here $\tilde{r} = r/R_g$, $\tilde{\ell} = \ell/R_g$,

$$\mu_*^2 = 1 - \left(\frac{R_{\rm li}}{R_g\tilde{x}}\right)^2 (1-\mu_{\rm re}^2)\ , \quad (124)$$

$$\tilde{x}^2 = \frac{R_{\rm li}^2 + \ell^2 - 2\ell R_{\rm li}\mu_{\rm re}}{R_g^2}\ , \quad (125)$$

and

$$\tilde{s} = \frac{\epsilon_{\rm li}\epsilon_1(1+z)(1-\mu_*)}{2}\ . \quad (126)$$

Similar calculations of $\gamma\gamma$ absorption by BLR photons have been done by Böttcher & Dermer (1995), Donea & Protheroe (2003), Reimer (2007), Dermer et al. (2009), and Böttcher & Els (2016).

For absorption by photons from a BLR ring, Equation (85),

$$\tau_{\gamma\gamma}(\epsilon_1) = 900\ \frac{\xi\ell_{\rm Edd}}{\epsilon_{\rm li}} \int_{\tilde{r}}^{\infty} \frac{d\tilde{\ell}}{\tilde{x}^2} \times \left(1 - \frac{\tilde{\ell}}{\tilde{x}}\right) \left[\frac{\sigma_{\gamma\gamma}(\tilde{s})}{\sigma_{\rm T}}\right] \quad (127)$$

where now

$$\tilde{x}^2 = \left(\frac{R_{\rm li}}{R_g}\right)^2 + \tilde{\ell}^2\ , \quad (128)$$

and

$$\tilde{s} = \frac{\epsilon_{\rm li}\epsilon_1(1+z)(1-\tilde{\ell}/\tilde{x})}{2}\ . \quad (129)$$

7.3. *Absorption by Dust Torus Photons*

For absorption of γ rays by photons from a dust torus, using the ring approximation for the dust torus, Equation (91),

$$\tau_{\gamma\gamma}(\epsilon_1) = 900\ \frac{\xi\ell_{\rm Edd}}{2.7\Theta} \int_{\tilde{r}}^{\infty} \frac{d\tilde{\ell}}{\tilde{x}^2} \left(1 - \frac{\tilde{\ell}}{\tilde{x}}\right) \times \left[\frac{\sigma_{\gamma\gamma}(\tilde{s})}{\sigma_{\rm T}}\right] \quad (130)$$

where here

$$\tilde{x}^2 = \left(\frac{R_{\rm dt}}{R_g}\right)^2 + \tilde{\ell}^2\ , \quad (131)$$

TABLE 3
Accretion Disk and Dust Torus Parameters

Parameter	Symbol	Value
Black hole mass [$M_\odot$]	$M_{\rm BH}$	1.2×10^9
Gravitational radius [cm]	$\rm R_g$	1.8×10^{14}
Disk luminosity [erg $\rm s^{-1}$]	$L_{\rm disk}$	2×10^{46}
Accretion efficiency	η	1/12
Inner disk radius [R_g]	$R_{\rm in}$	6
Outer disk radius [R_g]	$R_{\rm out}$	200
Dust torus temperature [K]	$T_{\rm dt}$	10^3
Dust torus scattering fraction	$\xi_{\rm dt}$	0.1
Dust torus (inner) radius [cm]	$R_{\rm dt,1}$	3.5×10^{18}
Dust torus (outer) radius [cm]	$R_{\rm dt,2}$	3.5×10^{19}
Dust torus cloud density gradient	ζ	1.0

and

$$\tilde{s} = \frac{2.7\Theta\epsilon_1(1+z)(1-\tilde{\ell}/\tilde{x})}{2}\ . \quad (132)$$

Using the extended dust torus model, Equation (101),

$$\tau_{\gamma\gamma}(\epsilon_1) = 900\ \frac{\xi\ell_{\rm Edd}}{2.7\Theta\tilde{R}_{\rm dt,eff}} \int_{\tilde{r}}^{\infty} d\tilde{\ell} \times \int_{R_{\rm dt,1}}^{R_{\rm dt,2}} \frac{d\tilde{R}_{\rm re}}{\tilde{x}^2} \left(1 - \frac{\tilde{\ell}}{\tilde{x}}\right) \left[\frac{\sigma_{\gamma\gamma}(\tilde{s})}{\sigma_{\rm T}}\right] \quad (133)$$

where now

$$\tilde{x}^2 = \left(\frac{R_{\rm re}}{R_g}\right)^2 + \tilde{\ell}^2 \quad (134)$$

and $\tilde{R}_{\rm dt,eff} = R_{\rm dt,eff}/R_g$.

Similar calculations of $\gamma\gamma$ absorption by interactions with dust torus photons have been done by Protheroe & Biermann (1997) and Donea & Protheroe (2003).

7.4. *The Escape of Gamma Rays*

In Figure 14 is plotted $\tau_{\gamma\gamma}$ versus photon energy E for photons from the accretion disk (Section 7.1), BLR (Section 7.2), and dust torus (Section 7.3), for γ rays originating at various distances r from the black hole. The BLR parameters are chosen to be consistent with 3C 454.3, as described in Appendix A. The accretion disk and dust torus parameters are given in Table 3. The black hole mass is consistent with that found for 3C 454.3 by Bonnoli et al. (2011, see the discussion therein), and the disk luminosity was chosen so that $L_{\rm disk} = 10L(5100\ \text{Å})$. Dust torus parameters are consistent with Equation (96). Note that energy (E) is in the frame of the galaxy, so that the observer sees absorption at energies a factor $(1+z)$ lower and that distances are given in terms of $R(\text{Ly}\alpha) = 1.1 \times 10^{17}$ cm.

Absorption by disk photons does not play a large role for the parameters explored here; they are important for > 5 TeV for the lowest value of r shown, where photons have not escaped anyway due to absorption by BLR and dust torus photons.

For $r < R(\text{Ly}\alpha)$, BLR absorption from Lyα dominates, although absorption by other lines is not negligible. At $r > R(\text{Ly}\alpha)$, other lines with larger radii dominate the BLR absorption. The flattened, ring geometry for the

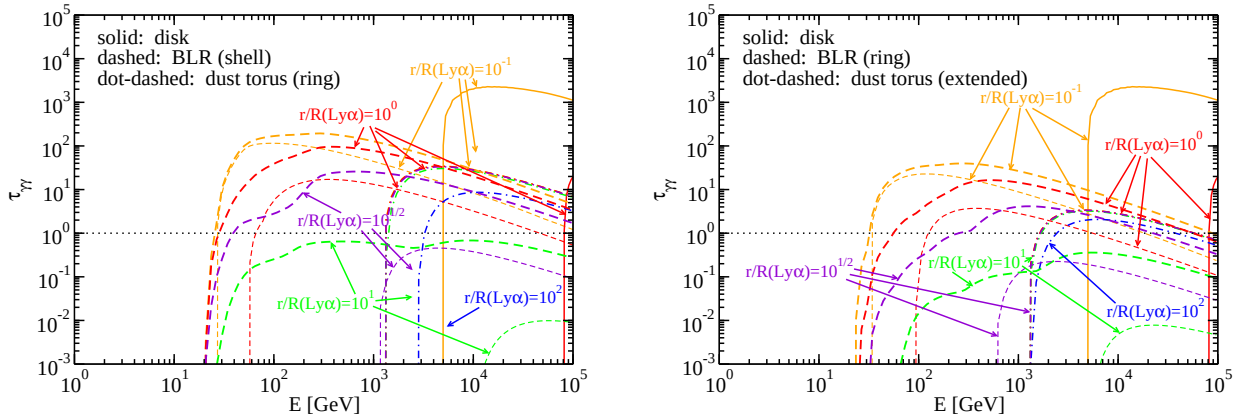

FIG. 14.— The $\gamma\gamma$ absorption optical depth from accretion disk photons (solid), BLR photons (dashed), and dust torus photons (dot-dashed). Absorption from all of the BLR line emission is given by the thick dashed curves, while absorption by only Lyα is given by the thin dashed curves. The dotted lines indicate $\tau_{\gamma\gamma} = 1$. *Left*: spherical shell BLR geometry and ring dust torus geometry. *Right*: ring BLR geometry and extended dust torus geometry.

BLR generally has lower $\tau_{\gamma\gamma}$, and requires a higher energy before pair production is important, as pointed out previously by Stern & Poutanen (2014). For distances $r > 10R(\mathrm{Ly}\alpha)$, $\tau_{\gamma\gamma} < 1$ from BLR photons, regardless of the geometry. Based on Figure 14, the detection of ≈ 60 GeV photons from 3C 454.3 (Pacciani et al. 2014) produced at $z = 0.859$ restricts their production to $r \gtrsim 10^1 R(\mathrm{Ly}\alpha) \approx 1.1 \times 10^{18}$ cm for a shell BLR geometry and $r \gtrsim 10^{1/2} R(\mathrm{Ly}\alpha) \approx 3.4 \times 10^{17}$ cm for a ring BLR geometry. Similar constraints can be made for other sources. Cutoffs in γ-ray spectra of FSRQs by BLR photons may have already been detected by the *Fermi*-LAT (Stern & Poutanen 2014). Those authors assume the cutoffs are due to absorption by Lyman continuum photons from the BLR (13.6 eV photons), which I do not consider since this feature is not included in the template by Vanden Berk et al. (2001); see Appendix A. The absorption of $\gtrsim 10$ GeV γ rays by BLR photons can have implications for using FSRQs to constrain the extragalactic background light (Reimer 2007).

Figure 14 shows that absorption by dust torus photons is mostly constant with r for $r \ll R_{\mathrm{dt}} \sim 10^2 R(\mathrm{Ly}\alpha)$. Above this value of r, the absorption by dust torus photons decreases for both the ring and extended geometries. The opacity is lower for the ring geometry, and pair production does not occur until slightly higher energies. If γ rays are produced at $r \ll R_{\mathrm{dt}}$, one does not expect to detect γ rays at $\gtrsim 1.3$ TeV for either the ring geometry or extended dust geometry, again, in the source frame. Indeed no γ rays have been detected at these energies from an FSRQ, despite several FSRQs having been detected by imaging atmospheric Cherenkov telescopes. This includes 3C 279 (Albert et al. 2008), 4C 21.35 (Aleksić et al. 2011), PKS 1510−089 (Abramowski et al. 2013), and PKS 1441+25 (Abeysekara et al. 2015; Ahnen et al. 2015). It has been announced that the FSRQ S4 0954+65 has been detected by MAGIC (Mirzoyan 2015), although the maximum energy at which it was detected is not yet public knowledge. These objects may have minor differences in parameters compared to those used to generate Figure 14, but differences are probably not too large.

8. LOCATION OF THE GAMMA-RAY EMITTING REGION

The dominant seed photon source for Compton scattering depends on the distance of the emitting region from the black hole. The EC flux at 1 GeV (in the observer's frame) as a function of the emitting region's distance from the black hole is plotted in Figure 15. For this plot, the accretion disk and dust torus parameters are given in Table 3. I plot only the Lyα line with parameters as described in Appendix A, although other lines contribute. Other parameters are taken from the modeling of 3C 454.3[2] by Cerruti et al. (2013b) in 2010 November, which they referred to as "epoch B". These parameters can be seen in Table 4. These authors use a (co-moving frame) log-parabola electron distribution described by

$$N'_e(\gamma') = N'_e(\gamma'_{pk}) \left(\frac{\gamma'}{\gamma'_{pk}} \right)^{-[2+b\log_{10}(\gamma'/\gamma'_{pk})]} , \quad (135)$$

and consequently, so do I in this section. Note that in Table 4, unlike Cerruti et al. (2013b), $N'_e(\gamma'_{pk})$ is in terms of absolute number of electrons rather than electron density. The only parameter that changes with time is r.

In Figure 15, one can see which radiation fields dominate the scattering process at different radii. At the lowest radii, scattering of disk radiation dominate. At $r \gtrsim 3{\times}10^{16}$ cm, scattering of the Lyα broad line begins to dominate. At $r \lesssim R(\mathrm{Ly}\alpha)$ the emission from scattering Lyα line radiation is approximately constant, although it decreases somewhat for the ring geometry. At $r \approx R(\mathrm{Ly}\alpha)$ there is an enhancement in scattering in the shell geometry, due to the proximity of the seed photons to the emitting region in this geometry, that is not present in the ring geometry. This enhancement was noted previously by several authors, (e.g., Ghisellini & Madau 1996; Donea & Protheroe 2003). For $r \gtrsim R(\mathrm{Ly}\alpha)$, the EC-Ly$\alpha$ flux decreases extremely rapidly, as $f_\epsilon \propto r^{-7.7}$ until

[2] This source has a redshift $z = 0.859$ giving it a luminosity distance $d_L = 5.5$ Gpc assuming a cosmology with $(h, \Omega_m, \Omega_\Lambda) = (0.7, 0.3, 0.7)$.

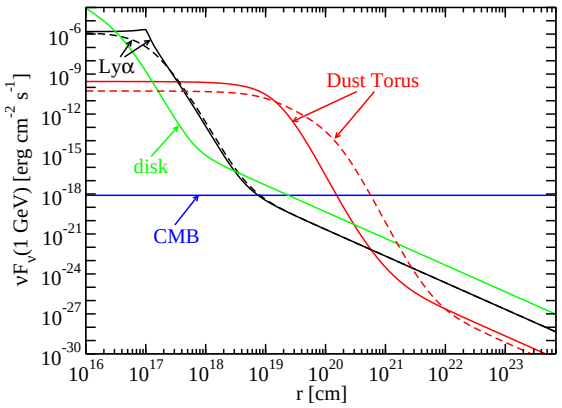

FIG. 15.— Plot of the νF_ν flux at 1 GeV (in the observer's frame) from Compton-scattering of various external radiation fields as a function of distance of the emitting region from the black hole. The seed photon radiation field is indicated on the plot. The solid black curve indicates a shell BLR geometry, while the dashed lack curve indicates a ring BLR geometry. The solid red curve indicates the ring dust torus geometry, while the dashed red curve indicates the extended dust torus geometry.

TABLE 4
JET PARAMETERS

Parameter	Symbol	Value
Lorentz factor	Γ	40
Doppler factor	$\delta_{\rm D}$	40
Magnetic Field [G]	B	0.56
ED[a] peak Lorentz factor	$\gamma'_{\rm pk}$	180
ED[a] normalization	$N'_e(\gamma'_{pk})$	2.4×10^{50}
ED[a] width parameter	b	1

[a] Electron Distribution

$r \approx 10^2 R({\rm Ly}\alpha)$ for both the shell and ring geometries. Above this radius, the BLR appears as a point source behind the jet, so that the flux decreases as $f_\epsilon \propto r^{-2}$. The EC-dust torus flux follows the same pattern for the ring geometry, as expected, except at larger radii. That is, it is $f_\epsilon \propto r^0$ for $r \lesssim R_{\rm dt}$; $f_\epsilon \propto r^{-7.7}$ for $R_{\rm dt} \lesssim r \lesssim 10^2 R_{\rm dt}$; and $f_\epsilon \propto r^{-2}$ for $10^2 R_{\rm dt} \lesssim r$. For the extended dust torus geometry, however, $f_\epsilon \propto \epsilon^{-2.5}$, between $R_{\rm dt,1}$ and $R_{\rm dt,2}$, decreasing more slowly than the ring geometry at these radii. With this dust torus model, Compton-scattering of dust torus radiation to produce γ rays is more viable at higher radii than the ring model. The scattering of the disk radiation field as a function of radius has been described previously by Dermer & Schlickeiser (2002). One consequence of this is that, at large radii ($r \gtrsim 3 \times 10^{20}$ cm ≈ 100 pc) the scattering of disk radiation actually dominates over scattering of Lyα line and dust torus radiation. However, this has little practical effect, as at these radii the scattering of diffuse CMB photons dominates over all other components shown on this plot.

For FSRQs, one expects that the nonthermal optical synchrotron and EC γ-ray emission is produced by approximately the same electrons. There is ample evidence of this in the correlation between optical and γ-ray variability in these objects (e.g. Chatterjee et al. 2012; Cohen et al. 2014; Ramakrishnan et al. 2016). An emitting region producing optical and γ rays is expected to be moving at high relativistic speeds ($\Gamma \gg 1$). If the emission originates from a region deep within the BLR, it quickly travels out of it, with external radiation fields becoming less geometrically favored for Compton scattering. Since the optical and γ-ray photons are produced by the same electrons, the observed γ rays should decrease relative to the optical. I compute the ratio of integrated γ-ray flux from EC processes to the optical (R band) flux density from synchrotron emission. For a blob traveling at constant velocity along the jet, its distance from the base of the jet at time to the observer $t_{\rm obs}$ is given by

$$r = r_0 + \frac{\beta c \delta_{\rm D} \Gamma \ (t_{\rm obs} - t_{\rm obs,0})}{1+z} \qquad (136)$$

assuming it is at a distance r_0 at $t_{\rm obs,0}$. Included are Compton scattering of accretion disk, BLR, and dust torus radiation. I include scattering of all of the lines described in Appendix A. Since the calculations are restricted to < 10 GeV, $\gamma\gamma$ absorption does not play a role, since there does not seem to be any absorption at < 10 GeV in FSRQs (Section 7). Synchrotron emission is calculated using formulae found in Crusius & Schlickeiser (1986) and Finke et al. (2008).

Results of this calculation can be seen in Figure 16. At first, the scattering of the accretion disk radiation dominates the γ-ray emission, but it quickly becomes very faint, within the first ≈ 0.25 hour. In the spherical shell geometry, as the blob approaches the radius of a particular line ($r \approx R_{\rm li}$) there is a peak in the flux, since there is essentially 0 distance between the blob and the photons source. This can be seen at $r \approx R({\rm Ly}\alpha) \approx 10^{17}$ cm. It can also be seen at later times where it approaches other shells, e.g., $r \approx 3 \times 10^{17}$ cm where it approaches the shell for the lines from C III, N III, Si IV, O IV], and especially C IV. There is another peak at $r \approx 5 \times 10^{17}$ cm where it approaches the shell for the ions for Lyβ and O VI. These peaks are not seen for the ring geometry, since with this geometry the blob does not approach the physical location where the lines are emitted. In general, the ring geometry results in less emission than the shell geometry. Comparing the decay for the ring dust torus model and extended dust torus model, clearly the extended dust torus model has lower flux, although it decays less rapidly, consistent with the results shown in Figure 15.

As the blob travels along the jet, the electron distribution will likely change. If the normalization but not the shape of the electron distribution changes (and the thermal accretion disk is not an important emission component), the ratio of γ-ray to optical flux as a function of time should follow the basic shape shown Figure 16. However, if the shape of the electron distribution changes, there could be additional variation in this ratio. In Figure 17 I plot the γ-ray flux to optical flux density ratio for the shell BLR and extended dust torus model for the same set of parameters (Table 4), but for both $b = 1.0$ and $b = 0.5$. The ratio clearly changes in response to changes in the electron distribution. However, changes due to this are small compared to the overall changes due to the falling external radiation field, where the ratio falls by many orders of magnitude within one

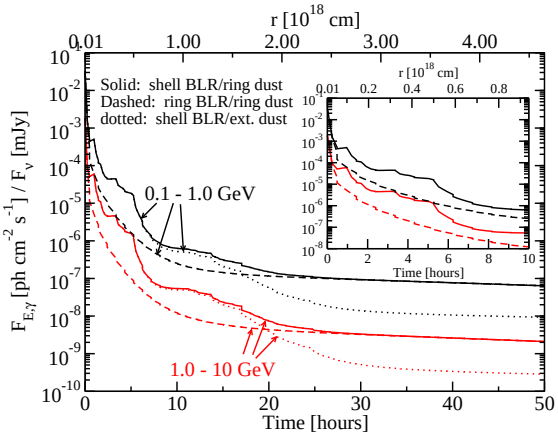

FIG. 16.— Predicted ratio of integrated γ-ray flux to R band flux density for a moving blob as a function of observed time. The energy range for the integrated γ-ray flux is indicated on the plot. Solid curves show results for a spherical shell BLR and ring dust torus; dashed curves show results for a ring BLR and ring dust torus; the dotted curves show results for a shell BLR and extended dust torus. The labels at the top display the distance of the blob from the base of the jet, r, at a given observer time. The inset shows the first 10 hours in more detail.

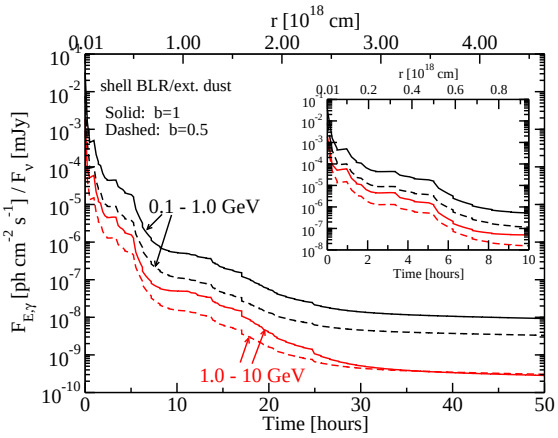

FIG. 17.— Same as Figure 16, for a shell BLR and extended dust torus model, but now plotting for different values of the log-parabola electron distribution parameter b.

day.

In Figure 18 these theoretical curves are plotted with the γ-ray to optical flux ratio as a function of time for the 2010 November flare in 3C 454.3. The LAT γ-ray data were previously presented by Abdo et al. (2011) and the Whole Earth Blazar Telescope (WEBT) optical data by Vercellone et al. (2011). These R band optical data were corrected for Galactic extinction using the model of Schlafly & Finkbeiner (2011), as found on the NASA Extragalactic Database[3]. The γ-ray time bins were 6 hours, and for most of these bins there were multiple WEBT data points, so in each 6-hour LAT time bin the WEBT data were averaged. Several of the LAT 6-hour bins did not have any optical data points in them, in which case the bin is not plotted. The flares were quite bright in both γ rays and optical; the latter indicates that contamination to the optical during the flare is likely to be

[3] https://ned.ipac.caltech.edu

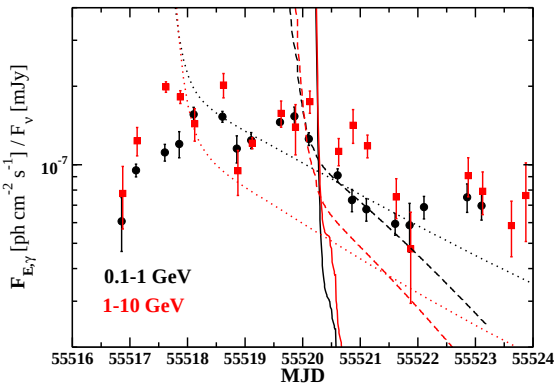

FIG. 18.— Ratio of integrated γ-ray flux to R band flux density observed during a flare from 3C 454.3 in 2010 November. The curves show the predictions from Figure 16. The energy range for the integrated γ-ray flux is indicated on the plot. Solid curves show results for a spherical shell BLR and ring dust torus. The dashed curves show this result adjusted to match the 0.1-1.0 GeV observations between MJD 55520 and MJD 55522. The dotted curves show the extended dust torus curve from Figure 16 adjusted to match the 0.1-1.0 GeV observations in the same time period. The 0.1-1 GeV data and curves have been multiplied by a factor 0.05.

minimal. The solid curves show the curves from Figure 18 with a shell BLR and ring dust torus adjusted so that $t = 0$ corresponds to MJD 55520.0. The blob rapidly moves out of the BLR so that these curves decay too quickly to explain the flare. If the flare occurs inside the BLR, it must be the result of a superposition of many different flaring regions, rather than a single region. A γ-ray sub-flare began on $\approx$ MJD 55519.0 that lasted until $\approx$ MJD 55522 (Abdo et al. 2011). Although this flare is too long to be explained by scattering of BLR photons in a single relativistically moving component, it may be explained by scattering of dust torus photons. Hence I also show the model adjusted to reproduce the ratio of the 0.1-1.0 GeV flux to the R band flux for the time period where the ratio is decaying, i.e., MJD 55520-MJD 55522 (the dashed black curve). In this case, the decay phase is described by the scattering of dust torus radiation. Once can see that the curve can indeed reproduce the decaying portion of this flare in the 0.1-1.0 GeV range. However, when the ratio of the 1.0-10.0 GeV flux to R band flux is adjusted by the same amount (red dashed curve) the curve clearly is not able to reproduce the observations. The γ-ray spectrum hardens during this decay phase, as noted by Abdo et al. (2011). The models with the extended dust torus are shown as the dotted curves, again adjusted to reproduce the ratio of 0.1-1.0 GeV flux to R band flux density observations in the entire MJD 55519-MJD 55522 range. The scattering of dust torus photons can reproduce the ratio of the 0.1-1.0 GeV flux, except for during MJD 55519.5-MJD 55520.0. Again, it does not also reproduce the 1.0-10.0 GeV curve.

My purpose here is not to reproduce the observed curves exactly, but to demonstrate that Compton scattering of dust torus photons by a single emitting jet component can in principle reproduce the entire sub-flare, from MJD 55519 to 55520, while scattering of disk or BLR photons by a single jet component cannot. Discrepancies between the dotted curves and the data could be explained by changes in other physical parameters in

the emitting region, such as the magnetic field or electron distribution parameters. Simple "one-zone" models where γ rays are created by Compton scattering of disk or BLR photons seem to be ruled out. More generally, EC models scattering dust torus photons with the extended dust torus model with $R_{\rm dt,2} = 10R_{\rm dt,1}$, as suggested by Nenkova et al. (2008a,b), should be viable for flares occurring at distances

$$r \lesssim R_{\rm dt,2} \approx 11\ L_{45}^{1/2}\ T_{\rm dt,3}^{-2.6}\ {\rm pc} \tag{137}$$

or lasting

$$\Delta t \lesssim 14\ \delta_{1.5}^{-2} \left[\frac{\delta_D}{\Gamma}\right]\ L_{45}^{1/2}\ T_{\rm dt,3}^{-2.6}\ (1+z)\ {\rm day} \tag{138}$$

where $\delta_{1.5} = \delta_{\rm D}/30$ and $L_{45} = L_{\rm disk}/(10^{45}\ {\rm erg\ s^{-1}})$. This is compatible with evidence that flares occur at these distances from the black hole in many FSRQs and BL Lacs. This includes γ-ray flares in 3C 279 at $r \approx 5$ pc (Abdo et al. 2010a), $r \approx 17$ pc PKS 1510−089 (Marscher et al. 2010), $r \approx 14$ pc in OJ 287 (Agudo et al. 2011a), $r \approx 12$ pc in AO 0235+164 (Agudo et al. 2011b), and $r \approx 10$ pc from PKS 1510−089 (Orienti et al. 2013). These flares could occur at the location of the 7 mm (43 GHz) core and still have γ-ray emission from Compton-scattering of dust photons, although if they occurred at much larger r, this scenario would not be viable. An

However, at these larger distances, the cooling timescale from Compton scattering of dust torus emission might be too long to explain the observed rapid decay in γ-ray flares. The energy density of photons from the dust torus can be estimated as

$$\begin{aligned} u'_{dt} &= \chi\ \frac{\Gamma^2 \xi_{\rm dt} L_{\rm disk}}{4\pi R_{\rm dt,1}^2 c} \\ &= 2.3\times10^{-5}\ \chi\ \xi_{\rm dt,-1}\ T_{\rm dt,3}\ {\rm erg\ cm^{-3}} \end{aligned} \tag{139}$$

where χ is a geometric factor taking into account the dust torus geometry and $\xi_{\rm dt,-1} = \xi_{\rm dt}/0.1$. The parameter $\chi = 1$ for the ring geometry with $r \ll R_{\rm dt}$. One can use Figure 15 to estimate $\chi = 0.01$ for the extended dust torus at $r = 10$ pc. Assuming $T_{\rm dt} \leq 2000$ K, the observer frame cooling timescale in the Thomson regime can be estimated at $r = 10$ pc as

$$\begin{aligned} t_{\rm cool} &= \frac{1+z}{\delta_{\rm D}} \frac{3m_e c^2}{4c\sigma_{\rm T} u'_{\rm dt} \gamma'} \\ &\geq 36\ (1+z)^{1/2}\ \chi_{-2}\ \delta_{1.5}^{-2}\ \left(\frac{\delta_{\rm D}}{\Gamma}\right)^2 \\ &\times \left(\frac{m_e c^2 \epsilon}{\rm GeV}\right)^{-1/2}\ {\rm hour} \end{aligned} \tag{140}$$

where $\chi_{-2} = \chi/0.01$. Abdo et al. (2011) find a falling timescale of 15 ± 2 hour for the γ-ray flare centered on MJD 55520. This would be marginally consistent with this cooling timescale for particularly large Doppler factors. On the other hand, the γ-ray flare from PKS 1510−089 around MJD 55850 has a falling timescale of 1.2 ± 0.15 hour (Brown 2013), which would be a problem if it was produced at 10 pc from the black hole, as suggested by Orienti et al. (2013). It might be possible to explain this rapid cooling by adiabatic losses.

9. SUMMARY

The location of the γ-ray emitting region is blazar jets is poorly known; modeling EC jet emission is necessary to determine its origin, but doing this correctly requires the full angle-dependent Compton cross-section. Consequently, I have created a novel δ-function approximation for Compton scattering that is fully angle dependent, valid in both the Thomson and extreme Klein-Nishina regimes. It assumes that all of the scattered photons have the same energy of the mean scattered photon. It allows one to eliminate an integral in Compton scattering calculations, so that in applications for scattering in blazar jets, it is numerically faster by up to approximately a factor of 10. It is likely to have applications to other high-energy astrophysical situations where accurate Compton scattering calculations are important.

I have used this approximation to derive formulae for Compton scattering of external radiation fields of interest to blazars; namely, external radiation originating from the accretion disk, BLR, and dust torus. The Compton-scattered accretion disk formula is essentially the same as the one from Dermer et al. (2009), only with the new approximation. Formulae for Compton-scattering of BLR photons are provided for two geometries, considering the line emission as originating from spherical shell and from a flat annulus. I have also provided a method for estimating the relative radii and luminosities of the various broad lines that make up the BLR (Appendix A). I also provide formulae for computing the scattering of dust torus photons using two dust torus models, one as a thin annulus, and one as an extended torus made up of many dust clouds. The latter is similar to the one described by Sikora et al. (2013), although I take into account the full angle dependence in the Compton-scattering calculation. I derive beaming patterns for scattering of spherical shell external radiation fields or annulus external radiation fields in the Thomson regime, the latter of which could represent either a broad emission line or a dust torus. I show that if the shell or annulus has a radius $R_{\rm re}$, then for distances $r \ll R_{\rm re}$, the beaming pattern resembles that of an isotropic radiation field; and for distances $r \gg R_{\rm re}$, it resembles the beaming pattern of a point source behind the jet. The beaming pattern for the spherical shell and annulus seed radiation field geometries are similar enough to each other that beaming pattern studies are unlikely to distinguish between them.

Using my models for radiation from the BLR and dust torus, I have computed the $\gamma\gamma$ absorption optical depth as a function of γ-ray energy and distance from the black hole. I believe these are the most detailed of this sort of calculation that has yet been performed. This calculation shows that photons below ≈ 20 GeV in the source frame are always able to escape unabsorbed. For γ rays emitted $r \gtrsim 10R({\rm Ly}\alpha)$, $\tau_{\gamma\gamma} < 1$ everywhere, at least for the fiducial parameters I used. For emission of γ rays in between these radii, the escape of γ rays is dependent on the details of the BLR structure, which I have realistically computed. The flattened, ring geometry lowers the opacity a bit, and the threshold is a bit higher, but the conclusions on the escape of γ rays are not changed drastically.

Finally, I explore the ratio of the Compton-scattered flux to synchrotron flux for a blob moving out in a jet.

This ratio, and how it changes with time, can be a clue to finding the location of the γ-ray emitting region. For flares lasting longer than $\sim$ a day, the flaring region rapidly moves out of the BLR (for fiducial values $\Gamma = \delta_D = 40$), so that scattering of BLR photons by a single blob cannot explain these flares, although emission by many separate blobs within the BLR would be possible. Scattering of photons from an extended dust torus at ~ 10 pc from the black hole is not able to cool photons fast enough to explain the rapid flares seen from FSRQs. If γ-ray flares originate from EC at these distances, another source of seed photons is needed to rapidly cool the electrons producing these flares. A possible alternative photon source is other regions of the jet: such as a sheath surrounding the emitting region (Ghisellini et al. 2005; MacDonald et al. 2015; Sikora et al. 2016) or scattering of photons from a standing shock or other moving regions of the jet (Marscher 2014). The location of the γ-ray emitting region in blazars and the seed photon source is still unclear.

In Section 8 I used data taken and assembled by the WEBT collaboration and stored in the WEBT archive at the Osservatorio Astrofisico di Torino-INAF[4]. I would particularly like to thank C. Raiteri for retrieving these data. This research has made use of the NASA/IPAC Extragalactic Database (NED) which is operated by the Jet Propulsion Laboratory, California Institute of Technology, under contract with the National Aeronautics and Space Administration. I am grateful to the anonymous referee for a prompt and helpful report, C. D. Dermer for useful discussions on Compton scattering, and C. Done who piqued my interest in beaming patterns for what became Section 6. I am funded by the Chief of Naval Research.

APPENDIX

A. SIMPLE EMPIRICAL STRATIFIED BROAD LINE REGION MODEL

There is a long history of using composite quasar templates to estimate the broad line luminosities and energy densities for blazars. For instance, Celotti et al. (1997); Liu & Bai (2006); and Joshi et al. (2014), among others, used the template from Francis et al. (1991); while Cerruti et al. (2013b) used the template from Telfer et al. (2002). When performing γ-ray Compton scattering or $\gamma\gamma$ absorption calculations, this has occasionally been criticized for not taking into account the stratification of the broad line region, with different lines being emitted at different radii (e.g., Poutanen & Stern 2010; Stern & Poutanen 2014). Here I present a method that uses the composite quasar spectrum from the SDSS (Vanden Berk et al. 2001) to estimate the radii where the lines are primarily emitted, along with the lines' luminosities.

Assume that there are two quasars, a and b, and each has two broad emission lines seen in their spectra, lines 1 and 2. Reverberation mapping indicates that the continuum luminosity at a particular wavelength (which can be different for each line) is proportional to the square of the broad line radius (e.g., Kaspi et al. 2005, 2007; Bentz et al. 2006, 2009, 2013), so that for line 1,

$$\frac{L_{a,1}}{L_{b,1}} = \left(\frac{R_{a,1}}{R_{b,1}}\right)^2 \tag{A1}$$

and similarly for line 2,

$$\frac{L_{a,2}}{L_{b,2}} = \left(\frac{R_{a,2}}{R_{b,2}}\right)^2 . \tag{A2}$$

Reverberation mapping is usually done for radio quiet AGN, but a handful of blazars have been the targets of reverberation mapping campaigns as well, and they seem to obey the same $L \propto R^2$ relation as radio quiet AGN (e.g., Kaspi et al. 2007). This is explained by photoionization, with lines emitting at primarily one radius where the ionization parameter and density are optimized (e.g., Wandel 1997; Wandel et al. 1999). Reverberation mapping for several objects also indicates that the broad line velocity width is related to the broad line radius as one would expect if the broad line clouds are in Keplerian orbits around the black hole (Peterson & Wandel 1999, 2000; Kollatschny 2003; Peterson et al. 2014), so that

$$\left(\frac{V_{a,1}}{V_{a,2}}\right)^2 = \frac{R_{a,2}}{R_{a,1}} \tag{A3}$$

and similarly for object b. Combining Equations (A1) through (A3) gives

$$\left(\frac{V_{a,1}}{V_{a,2}}\right)^2 = \frac{R_{a,2}}{R_{a,1}} = \frac{R_{b,2}}{R_{b,1}} \left(\frac{L_{a,2}}{L_{a,1}}\right)^{1/2} \left(\frac{L_{b,1}}{L_{b,2}}\right)^{1/2} \tag{A4}$$

If the continuum luminosities at different wavelengths for a certain object are directly proportional to each other,i.e.,

[4] http://www.oato.inaf.it/blazars/webt/

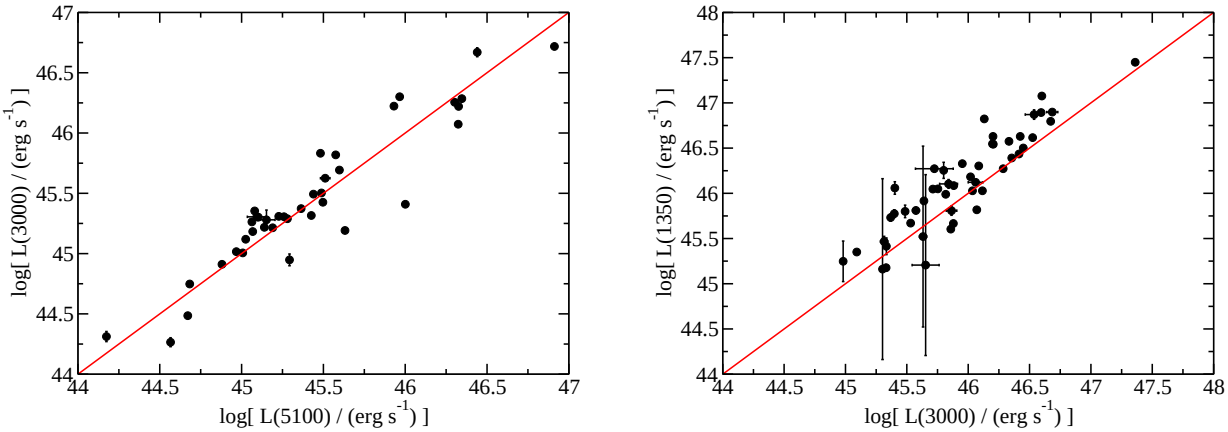

FIG. 19.— Continuum luminosities of FSRQs at different wavelengths, plotted against each other. Data are from from Shaw et al. (2012). *Left*: Luminosities at 3000 Å versus 5100 Å. *Right*: Luminosities at 1350 Å versus 3000 Å. The red lines show where the luminosities are equal.

if $L_{a,1} \propto L_{a,2}$ and $L_{b,1} \propto L_{b,2}$, then

$$\left(\frac{V_{a,1}}{V_{a,2}}\right)^2 = \frac{R_{a,2}}{R_{a,1}} = \frac{R_{b,2}}{R_{b,1}} = \left(\frac{V_{b,1}}{V_{b,2}}\right)^2 \tag{A5}$$

and the ratios of radii for different lines are proportional to each other. In Figure 19 I plot the optical/UV continua for FSRQs, taken from Shaw et al. (2012), against each other. Not only does it seem that $L_{a,1} \propto L_{a,2}$, it appears that $L_{a,1} \approx L_{a,2}$, as a first order approximation, although the scatter is quite large.

Reverberation mapping is expensive in terms of telescope time; it has only been performed for a limited number of objects and lines. Still, if one assumes that the empirical results represented by Equations (A1) through (A5) are correct for *all* broad lines and quasars, one can use the composite quasar spectral template from Vanden Berk et al. (2001) to estimate the relative luminosities, line velocity widths, radii, and energy densities for $r < R_{\rm li}$,

$$u = \frac{L_{\rm li}}{4\pi c R_{\rm li}^2} \ , \tag{A6}$$

for all lines in the template. This is done in Table 5 for all lines in the template [see Table 2 of Vanden Berk et al. (2001)] with $V > 1000$ km s^{-1}. All results are in terms of Hβ, the most common line used for reverberation mapping. If one assumes the Vanden Berk et al. (2001) template is representative of a quasar with a "composite mass", and the other assumptions stated above are correct, then these ratios should be approximately correct for *every* quasar. This may also be justified by noting that composite SDSS quasar spectra, binned by luminosity, are very similar (Vanden Berk et al. 2004).

How do the results compare with the results of reverberation mapping campaigns? Few campaigns have been performed on lines other than Hβ, so comparisons are limited. A comparison of Si IVλ1400 and C IVλ1549 give comparable radii, within a factor of 2. The lines C III]λ1909, and He IIλ4686 fare worse, off by factors of about 3 and $\gtrsim 80$, respectively. A comparison of He Iλ5876 with Kollatschny (2003) also fares poorly, off by a factor of $\gtrsim 8$. The poor agreement may be because the luminosities for these lines are more faint, making it difficult to measure their widths. In this case, it seems likely that the stronger lines in Table 5 are reliable within a factor of 2 or so, while the weaker ones are completely unreliable. Due to the poor agreement, I replaced the results for He IIλ4686 and He Iλ5876 in Table 5 with those from Peterson & Wandel (1999) and Kollatschny (2003). The luminosities and velocity widths from Table 5 can also be compared with those found for FSRQs by, for example, Pian et al. (2005) and Shaw et al. (2012). Although errors for individual objects are large, agreement with the means of these parameters is good, within about a factor of 2.

For NGC 5548, reverberation mapping indicates $R(\mathrm{Ly}\alpha) \approx 6$ light-days (De Rosa et al. 2015) and $R(\mathrm{H}\beta) \approx 20$ light-days (Peterson & Wandel 1999), a ratio in approximate agreement with Table 5 (0.30 versus 0.26). This is perhaps the most reassuring, since Lyα is the brightest line with the greatest energy density, due to its compactness and brightness. It is the most important line for the purposes of Compton scattering and $\gamma\gamma$ absorption for $r < R(\mathrm{Ly}\alpha)$.

As an example, one can consider the well-known γ-ray emitting quasar 3C 454.3. According to Isler et al. (2013), the luminosity of Hβ is $L(\mathrm{H}\beta) = (4.2 \pm 1.6) \times 10^{43}$ erg s^{-1}. Using the relation from Greene & Ho (2005),

$$\left(\frac{L(5100\ \text{Å})}{10^{44}\ \text{erg s}^{-1}}\right) = \left(\frac{L(\mathrm{H}\beta)}{(1.425 \pm 0.007) \times 10^{42}\ \text{erg s}^{-1}}\right)^{0.8826 \pm 0.0039} \ , \tag{A7}$$

TABLE 5
Broad Emission Line Parameters

Ion	λ [Å]	$L/L(H\beta)$	$V/V(H\beta)$	$R/R(H\beta)$	$u/u(H\beta)$
Lyϵ	937.80	0.24	0.61	2.7	0.033
Lyδ	949.74	0.24	0.60	2.8	0.031
C III	977.02	0.60	1.1	0.83	0.88
N III	990.69	0.60	1.1	0.85	0.83
Lyβ	1025.72	1.1	0.91	1.2	0.76
O VI	1033.83	1.1	0.90	1.2	0.73
Ar I	1066.66	0.094	0.47	4.5	0.0046
Lyα	1215.67	12	1.9	0.27	160
O I	1304.35	0.23	0.50	4.0	0.014
Si II	1306.82	0.23	0.50	4.0	0.014
Si IV	1396.76	1.0	1.1	0.83	1.5
O IV]	1402.06	1.0	1.1	0.83	1.5
C IV	1549.06	2.9	1.1	0.83	4.2
N IV	1718.55	0.030	0.51	3.8	0.0021
Al II	1721.89	0.030	0.51	3.8	0.0021
C III]	1908.73	1.8	1.5	0.46	8.9
[Ne IV]	2423.83	0.051	0.42	5.8	0.0015
Mg II	2798.75	1.7	1.5	0.45	8.6
He I	3188.67	0.051	0.48	4.3	0.003
Hδ	4102.89	0.12	0.55	3.4	0.011
Hγ	4341.68	0.30	0.56	3.2	0.030
He II[a]	4687.02	0.016	2.5	0.63	0.040
Hβ	4862.68	1.0	1.0	1.0	1.0
[Cl III]	5539.43	0.039	0.46	4.8	0.0027
He I[a]	5877.29	0.092	1.6	0.39	0.60
Hα	6564.61	3.6	0.87	1.3	2.0

[a] Velocities and radii for these lines come from Peterson & Wandel (1999) and Kollatschny (2003).

one gets $L(5100\ \text{Å}) = (2.0 \pm 0.7) \times 10^{45}$ erg s^{-1} for the continuum luminosity at 5100 Å. Using the relation for the radius where Hβ is primarily emitted (Bentz et al. 2013),

$$R(\mathrm{H}\beta) = 10^{16.94\pm0.03} \left(\frac{L(5100\ \text{Å})}{10^{44}\ \text{erg s}^{-1}}\right)^{0.533\pm0.035} \text{cm} , \tag{A8}$$

one gets $R(\mathrm{H}\beta) = (4.3 \pm 0.2) \times 10^{17}$ cm. The energy density of Hβ photons inside $R(\mathrm{H}\beta)$ is then

$$u(\mathrm{H}\beta) = \frac{L(\mathrm{H}\beta)}{4\pi c[R(\mathrm{H}\beta)]^2} = (6.0 \pm 2.4) \times 10^{-4}\ \text{erg cm}^{-3} . \tag{A9}$$

One can then estimate the luminosities, radii, and energy densities of other broad lines using Table 5.

REFERENCES

Abdo, A. A., et al. 2010a, Nature, 463, 919
—. 2010b, ApJ, 716, 30
—. 2011, ApJ, 733, L26
Abeysekara, A. U., et al. 2015, ApJ, 815, L22
Abramowski, A., et al. 2013, A&A, 554, A107
Acero, F., et al. 2015, ApJS, 218, 23
Agudo, I., et al. 2011a, ApJ, 726, L13
—. 2011b, ApJ, 735, L10
Ahnen, M. L., et al. 2015, ApJ, 815, L23
Albert, J., et al. 2008, Science, 320, 1752
Aleksić, J., et al. 2011, ApJ, 730, L8
Becker, P. A., & Kafatos, M. 1995, ApJ, 453, 83
Bentz, M. C., Peterson, B. M., Netzer, H., Pogge, R. W., & Vestergaard, M. 2009, ApJ, 697, 160
Bentz, M. C., Peterson, B. M., Pogge, R. W., Vestergaard, M., & Onken, C. A. 2006, ApJ, 644, 133
Bentz, M. C., et al. 2013, ApJ, 767, 149
Błażejowski, M., Sikora, M., Moderski, R., & Madejski, G. M. 2000, ApJ, 545, 107
Bloom, S. D., & Marscher, A. P. 1996, ApJ, 461, 657
Blumenthal, G. R., & Gould, R. J. 1970, Reviews of Modern Physics, 42, 237
Bonnoli, G., Ghisellini, G., Foschini, L., Tavecchio, F., & Ghirlanda, G. 2011, MNRAS, 410, 368
Böttcher, M. 2014, ApJ, 795, 35
Böttcher, M., & Bloom, S. D. 2000, AJ, 119, 469
Böttcher, M., & Dermer, C. D. 1995, A&A, 302, 37
Böttcher, M., Dermer, C. D., & Finke, J. D. 2008, ApJ, 679, L9
Böttcher, M., & Els, P. 2016, ApJ, 821, 102
Böttcher, M., Mause, H., & Schlickeiser, R. 1997, A&A, 324, 395
Böttcher, M., Reimer, A., Sweeney, K., & Prakash, A. 2013, ApJ, 768, 54
Brown, A. M. 2013, MNRAS, 431, 824
Brown, R. W., Mikaelian, K. O., & Gould, R. J. 1973, Astrophys. Lett., 14, 203
Celotti, A., Padovani, P., & Ghisellini, G. 1997, MNRAS, 286, 415
Cerruti, M., Boisson, C., & Zech, A. 2013a, A&A, 558, A47
Cerruti, M., Dermer, C. D., Lott, B., Boisson, C., & Zech, A. 2013b, ApJ, 771, L4
Cerruti, M., Zech, A., Boisson, C., & Inoue, S. 2015, MNRAS, 448, 910
Chatterjee, R., et al. 2012, ApJ, 749, 191
Cohen, D. P., Romani, R. W., Filippenko, A. V., Cenko, S. B., Lott, B., Zheng, W., & Li, W. 2014, ApJ, 797, 137
Coppi, P. S., & Blandford, R. D. 1990, MNRAS, 245, 453
Crusius, A., & Schlickeiser, R. 1986, A&A, 164, L16
De Rosa, G., et al. 2015, ApJ, 806, 128
Decarli, R., Dotti, M., & Treves, A. 2011, MNRAS, 413, 39
Dermer, C. D. 1995, ApJ, 446, L63+

Dermer, C. D., Finke, J. D., Krug, H., & Böttcher, M. 2009, ApJ, 692, 32
Dermer, C. D., & Menon, G. 2009, High Energy Radiation from Black Holes: Gamma Rays, Cosmic Rays, and Neutrinos
Dermer, C. D., & Schlickeiser, R. 1993, ApJ, 416, 458
—. 2002, ApJ, 575, 667
Dermer, C. D., Schlickeiser, R., & Mastichiadis, A. 1992, A&A, 256, L27
Donea, A., & Protheroe, R. J. 2003, Astroparticle Physics, 18, 377
Dubus, G., Cerutti, B., & Henri, G. 2008, A&A, 477, 691
—. 2010, A&A, 516, A18
Finke, J. D., & Becker, P. A. 2015, ApJ, 809, 85
Finke, J. D., Dermer, C. D., & Böttcher, M. 2008, ApJ, 686, 181
Francis, P. J., Hewett, P. C., Foltz, C. B., Chaffee, F. H., Weymann, R. J., & Morris, S. L. 1991, ApJ, 373, 465
Gardner, E., & Done, C. 2014, MNRAS, 438, 779
Georganopoulos, M., Kirk, J. G., & Mastichiadis, A. 2001, ApJ, 561, 111
Ghisellini, G., & Madau, P. 1996, MNRAS, 280, 67
Ghisellini, G., Tavecchio, F., & Chiaberge, M. 2005, A&A, 432, 401
Gould, R. J., & Schréder, G. P. 1967, Physical Review, 155, 1404
Greene, J. E., & Ho, L. C. 2005, ApJ, 630, 122
Gupta, S., Böttcher, M., & Dermer, C. D. 2006, ApJ, 644, 409
Hunger, L., & Reimer, A. 2016, A&A, 589, A96
Hutter, A., & Spanier, F. 2011, Advances in Space Research, 48, 1415
Isler, J. C., et al. 2013, ApJ, 779, 100
Jamil, O., & Böttcher, M. 2012, ApJ, 759, 45
Jauch, J. M., & Rohrlich, F. 1976, The theory of photons and electrons. The relativistic quantum field theory of charged particles with spin one-half
Jones, F. C. 1968, Physical Review, 167, 1159
Joshi, M., Marscher, A. P., & Böttcher, M. 2014, ApJ, 785, 132
Kaspi, S., Brandt, W. N., Maoz, D., Netzer, H., Schneider, D. P., & Shemmer, O. 2007, ApJ, 659, 997
Kaspi, S., Maoz, D., Netzer, H., Peterson, B. M., Vestergaard, M., & Jannuzi, B. T. 2005, ApJ, 629, 61
Kataoka, J., et al. 1999, ApJ, 514, 138
Kollatschny, W. 2003, A&A, 407, 461
Landt, H., Padovani, P., Perlman, E. S., & Giommi, P. 2004, MNRAS, 351, 83
Laor, A., & Netzer, H. 1989, MNRAS, 238, 897
Liu, H. T., & Bai, J. M. 2006, ApJ, 653, 1089
Lu, W., Kumar, P., & Smoot, G. F. 2015, MNRAS, 453, 1458
MacDonald, N. R., Marscher, A. P., Jorstad, S. G., & Joshi, M. 2015, ApJ, 804, 111
Mankuzhiyil, N., Ansoldi, S., Persic, M., & Tavecchio, F. 2011, ApJ, 733, 14
Mankuzhiyil, N., Persic, M., & Tavecchio, F. 2010, ApJ, 715, L16
Marcha, M. J. M., Browne, I. W. A., Impey, C. D., & Smith, P. S. 1996, MNRAS, 281, 425
Marscher, A. P. 2014, ApJ, 780, 87
Marscher, A. P., et al. 2010, ApJ, 710, L126
McLure, R. J., & Dunlop, J. S. 2001, MNRAS, 327, 199
Meyer, E. T., Georganopoulos, M., Sparks, W. B., Godfrey, L., Lovell, J. E. J., & Perlman, E. 2015, ApJ, 805, 154
Mirzoyan, R. 2015, The Astronomer's Telegram, 7080, 1
Moderski, R., Sikora, M., Coppi, P. S., & Aharonian, F. 2005, MNRAS, 363, 954
Nenkova, M., Sirocky, M. M., Ivezić, Ž., & Elitzur, M. 2008a, ApJ, 685, 147
Nenkova, M., Sirocky, M. M., Nikutta, R., Ivezić, Ž., & Elitzur, M. 2008b, ApJ, 685, 160
Netzer, H. 2015, ARA&A, 53, 365
Orienti, M., et al. 2013, MNRAS, 428, 2418
Pacciani, L., Tavecchio, F., Donnarumma, I., Stamerra, A., Carrasco, L., Recillas, E., Porras, A., & Uemura, M. 2014, ApJ, 790, 45
Peterson, B. M., & Wandel, A. 1999, ApJ, 521, L95
—. 2000, ApJ, 540, L13
Peterson, B. M., et al. 2014, ApJ, 795, 149
Petropoulou, M., & Dermer, C. D. 2016, ApJ, 825, L11
Petropoulou, M., & Dimitrakoudis, S. 2015, MNRAS, 452, 1303
Pian, E., Falomo, R., & Treves, A. 2005, MNRAS, 361, 919
Poutanen, J., & Stern, B. 2010, ApJ, 717, L118
Press, W. H., Teukolsky, S. A., Vetterling, W. T., & Flannery, B. P. 1992, Numerical recipes in C. The art of scientific computing (Cambridge: University Press, —c1992, 2nd ed.)
Protheroe, R. J., & Biermann, P. L. 1997, Astroparticle Physics, 6, 293
Ramakrishnan, V., et al. 2016, MNRAS, 456, 171
Reimer, A. 2007, ApJ, 665, 1023
Reimer, A., Pohl, M., & Reimer, O. 2006, ApJ, 644, 1118
Reynolds, S. P. 1982, ApJ, 256, 38
Sanchez, D. A., et al. 2015, MNRAS, 454, 3229
Schlafly, E. F., & Finkbeiner, D. P. 2011, ApJ, 737, 103
Shakura, N. I., & Sunyaev, R. A. 1973, A&A, 24, 337
Shaw, M. S., et al. 2012, ApJ, 748, 49
Sikora, M., Begelman, M. C., & Rees, M. J. 1994, ApJ, 421, 153
Sikora, M., Janiak, M., Nalewajko, K., Madejski, G. M., & Moderski, R. 2013, ApJ, 779, 68
Sikora, M., Rutkowski, M., & Begelman, M. C. 2016, MNRAS, 457, 1352
Sikora, M., Stawarz, Ł., Moderski, R., Nalewajko, K., & Madejski, G. M. 2009, ApJ, 704, 38
Stern, B. E., & Poutanen, J. 2014, ApJ, 794, 8
Telfer, R. C., Zheng, W., Kriss, G. A., & Davidsen, A. F. 2002, ApJ, 565, 773
Vanden Berk, D., Yip, C., Connolly, A., Jester, S., & Stoughton, C. 2004, in Astronomical Society of the Pacific Conference Series, Vol. 311, AGN Physics with the Sloan Digital Sky Survey, ed. G. T. Richards & P. B. Hall, 21
Vanden Berk, D. E., et al. 2001, AJ, 122, 549
Vercellone, S., et al. 2011, ApJ, 736, L38
Wandel, A. 1997, ApJ, 490, L131
Wandel, A., Peterson, B. M., & Malkan, M. A. 1999, ApJ, 526, 579
Yan, D., Zeng, H., & Zhang, L. 2012, MNRAS, 424, 2173
Yan, D., Zhang, L., Yuan, Q., Fan, Z., & Zeng, H. 2013, ApJ, 765, 122
Zacharias, M., & Wagner, S. J. 2016, A&A, 588, A110
Zdziarski, A. A., & Böttcher, M. 2015, MNRAS, 450, L21
Zdziarski, A. A., Stawarz, Ł., Pjanka, P., & Sikora, M. 2014, MNRAS, 440, 2238
Zhang, S. N., Cui, W., & Chen, W. 1997, ApJ, 482, L155